Collision geometry and particle production in high energy heavy ion collision experiments*

WANG Ya-Ping(王亚平)[1)] ZHOU Dai-Mei(周代梅)[2)] HUANG Rui-Dian(黄瑞典) CAI Xu(蔡勖)[3)]

(Institute of Particle Physics, Central China Normal University, Wuhan 430079, China)

Abstract An overview of research status of soft physics in high energy heavy-ion collision experiments and recent experimental results are presented. This paper includes four parts: 1) Theoretical predictions of quark-gluon plasma and introduction for high energy heavy ion collision experiments. 2) Experimental status on collision geometry. 3) Experimental status on particle production. 4) Conclusion and outlook for research status of soft physics in LHC/ALICE.

Key words quark-gluon plasma (QGP), soft physics, collision geometry, particle production

PACS 25.75.-q

1 Introduction

The 19th International Conference on Ultra-Relativistic Nucleus-Nucleus Collisions (QM2006) was held in Shanghai, China on November 14—20, 2006. In the conference, relativistic heavy ion collider (RHIC) experiments (including BRAHMS, PHENIX, PHOBOS and STAR collaborations) at Brookhaven National Laboratory (BNL) gave many further surprising results from experimental data, and large hadron collider (LHC) experiments (including ALICE, ATLAS, CMS and LHCb collaborations) at European Organization for Nuclear Research (CERN) reported the progress & status of LHC and gave many prospective physics results of searching for Quark-Gluon Plasma (QGP). Also, the Super Proton Synchrotron (SPS) experiments at CERN and the Institute for Heavy Ion Research (GSI) collaborations presented their results and new plan. More than 700 theorists and experimentalists participated in the exciting conference.

In April 2005, the four experimental collaborations at RHIC announced jointly[1—4] that the RHIC had discovered a "perfect liquid" in high energy Au+Au collisions. The new state of nuclear matter behaviors like a liquid, not like a gas of free quarks and gluons. This matter interacts much more strongly than originally expected, thus theorists gives it a new name "sQGP" (strongly interacting QGP). Dr. T. D. Lee said, "The discovery of the strongly interacting quark-gluon plasma is a historical event."

1.1 Theoretical prediction: phase transition between QCD and QGP states

The goal of the experimental heavy ion program at ultra-relativistic energies is to study Quantum Chromo-Dynamics (QCD) in an environment very different from that encountered in hard processes, in a dense system of quarks and gluons[5].

The lattice calculations of QCD predict that nuclear matter undergoes a phase transition from hadron state to a deconfined state of QGP at a critical temperature T_c, corresponding to an energy density of ε_c. The dissolution of massive hadrons into almost massless quarks and gluons at T_c leads to a very rapid rise of the energy density near the deconfinement transition, as shown[6] in Fig. 1.

In Fig. 1, the curves labeled "2 flavours" and "3 flavours" were calculated for two and three light quark flavours of mass m_q/T=0.4, respectively. "2+1 flavours" indicates a calculation for two light and one heavier strange quark flavours of m_q/T=1[8]. In this

Received 21 May 2007

* Supported by Ministry of Education of China (306022) and National Natural Science Foundation of China (10635020)

1) E-mail: wangyp@iopp.ccnu.edu.cn

2) E-mail: zhoudm@phy.ccnu.edu.cn

3) E-mail: xcai@mail.ccnu.edu.cn

case the ratio ε/T^4 interpolates between two light flavours at $T \lesssim T_c$ and three light flavours at $T \gtrsim 2T_c$. For 2 and 2+1 flavours the critical temperature is T_c=173±15 MeV[7]. The arrows on the right-side ordinates show the value of the Stefan-Boltzmann limit for an ideal quark-gluon gas.

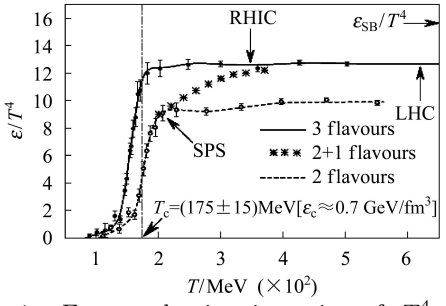

Fig. 1. Energy density in units of T^4 for QCD with two and three dynamical quark flavours[7].

A contribution to ε/T^4, which is directly proportional to the quark masses and thus vanishes in the massless limit, has been ignored in these curves. Since the strange quarks have a mass $m_s \approx T_c$ they will not contribute the thermodynamics close to T_c but will do so at higher temperatures[6]. Bulk thermodynamic observable of QCD with a realistic quark-mass spectrum thus will essentially be given by massless 2-flavour QCD close to T_c and will rapidly switch over to the thermodynamics of massless 3-flavor QCD in the QGP phase.

1.2 Heavy-ion collision experiments at high energies

Searching for new physics in heavy ion collisions requires a detailed understanding of elementary nucleon-nucleon collision. As hydrodynamical theory, we can divide typically the collision process into three basic stages: initial conditions, hydrodynamic evolution (hard interactions and quark-gluon plasma) and freeze-out. After collisions, medium of high energy density and high temperature is created, with very high particle yields. Thus, it's significant that what we can see from "ashes" of the medium.

The left panel of Fig. 2 shows inclusive charged particle transverse momentum (p_T) spectra obtained from p-p collisions at the Intersecting Storage Rings (ISR)[9], and from p-$\bar{p}$ collisions by UA1[10] at CERN, and by the Collider Detector at Fermilab (CDF)[11] at Fermi National Accelerator Laboratory (FNAL). With beam energy increasing high p_T particle production is enhanced which reflects the increase of the jet production cross-section.

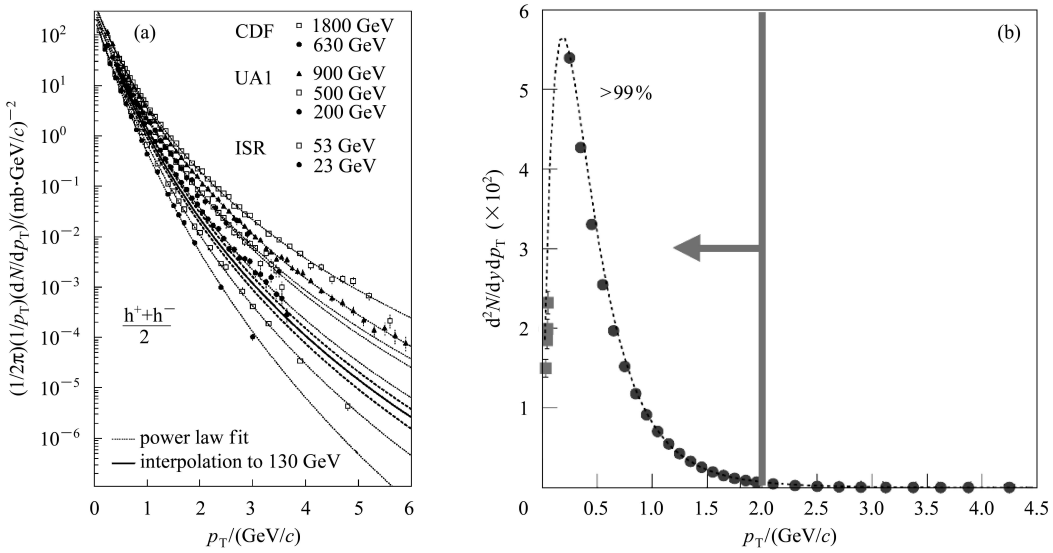

Fig. 2. (a) Inclusive charged particle production for p-p and p-$\bar{p}$ collisions[9—11]. (b) Schematic drawing of soft particle production.

In hadron-hadron reactions, hard scattering followed by fragmentation is considered to be the dominant process of hadron production for particles with p_T >2 GeV/c at mid-rapidity. At low transverse momentum, where particles have p_T <2 GeV/c, particle interactions are often referred to as "soft"[4]. The right panel of Fig. 2 shows the soft particles production spectrum. As it shows, the soft particles, with small momentum transferred and p_T <2 GeV/c, take more than 99% of the total particle yields.

1.3 Framework of the paper

This series of review are interested in research status of soft physics in high energy heavy ion collision experiments. As the first part of the review, this paper will give an overview of global properties of soft

physics, including collision geometry and particle production. This paper gives detailed description for these parts in Section 2 and 3, respectively. At last, the paper will give a conclusion for the status and an outlook for LHC experiments on soft physics. The following parts of the review will concentrate on the properties of hadronization, thermodynamics, correlations and fluctuation presented by Prof. D. M. Zhou, Y. P. Wang et al[12]. We suggest the readers refer to an overview entitled "Experimental Status of Ultra-High Energy Induced Nuclear Reactions" presented by X. Cai[13].

2 Collision geometry

The collision geometry (i.e. the impact parameter b) determines the number of participating nucleons $N_{\rm part}$, and many observables in experiments are scaled with $N_{\rm part}$, such as transverse energy, particle multiplicity, particle spectra and so on. The mean number of participating nucleons ($\langle N_{\rm part}\rangle$) can be estimated by ($A$-$N_{\rm spec}$) , and the number of spectators $N_{\rm spec}$ is measured by Zero-Degree Calorimeter (ZDC) apparatus. The mean number of binary nucleon-nucleon collisions ($\langle N_{\rm coll}\rangle$) can be estimated using Monte-Carlo methods. we know that the smaller b, the more participants $N_{\rm part}$, then the bigger collision system will be produced with higher particle yields.

2.1 Hydrodynamics description of high energy collisions

One of the major surprises from the RHIC data[1—4] has been the relevance of relativistic hydrodynamics in the overall understanding of the experimental data. The relevant geometry in the early stages of a heavy-ion collision or a p-p collision is one characterized by the nuclear radius in the transverse direction, and a large contraction in the longitudinal direction. We already see the relevant time scales for longitudinal and transverse dynamics are very different, of order $\tau_{\rm T}\approx R/c$, (approximately several fm/c) in the transverse direction and $\tau_{\rm L}\approx mR/(c_{\rm s}\sqrt{s})(\ll$ 1 fm/c) in the longitudinal direction[14].

2.1.1 Landau hydrodynamics model

Fermi and Landau considered a system with the geometry just described above, replacing the potential complexities of a high energy nuclear collision with a slab of area πR^2 and length $\Delta = mR/\sqrt{s}$ (and thus volume $V\propto R^3/\sqrt{s_{\rm NN}}$) in which all of the energy of the incoming projectiles is assumed to thermalize. In a nuclear collision, the total entropy in the collision volume is S, $S\propto V\propto N_{\rm part}$, leading to the $N_{\rm part}$-scaling of total multiplicities. This statistical model was extended by Landau with using the equations of relativistic hydrodynamics[15, 16]. It turns out that the strong compression along one axis leads to highly anisotropic distributions, with the Gaussian rapidity distributions of width $\sigma=\ln\sqrt{s/m^2}$. It is the application of the Fermi-Landau initial conditions to the generally-accepted formalism of 3D relativistic hydrodynamics that is the known as the "Landau hydrodynamics model".

The existing data are broadly well consistent with Landau's original predictions from the 1950's, as shown[14] in Fig. 3. However, the Landau model starts with a static initial state and rapidly generates the rapidity distribution by means of hydrodynamics. So, $\mathrm{d}N_{\rm ch}/\mathrm{d}\eta$ is not a static "initial-state" effect, but rather the result of a dynamical process in the very first stages of the collision.

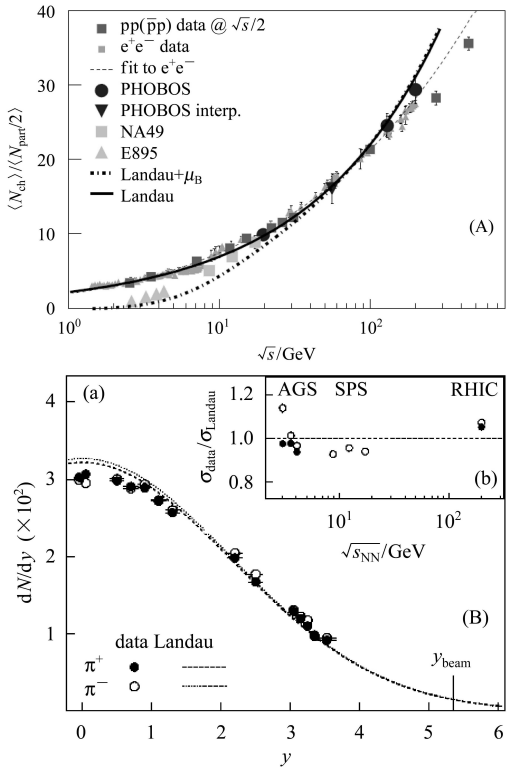

Fig. 3. (A) $N_{\rm ch}$ compared for A-A, e^+-e^- and p-p collisions[17, 18]. (B) BRAHMS data $\mathrm{d}N/\mathrm{d}y$ for charged pions at 200 GeV, fit to a Gaussian. The inset shows the width divided by the Landau expectation as a function of $\sqrt{s_{\rm NN}}$[19].

2.1.2 Bjorken hydrodynamics model

Landau hydrodynamics seems to be relevant to the physics in the very early stages ($\tau\ll 1$ fm/c). By contrast, hydrodynamic calculations which assume boost-invariance in the initial conditions have been used for quantitative comparisons with experimental observables that are sensitive to early-time pressure gradients[20]. These models are presented by Bjorken[21], who postulated the imposition of boost-

invariance[22] as a guiding principle for high energy interactions. Since the calculations are initialized at time scales on the order of 1 fm/c, they are unable to calculate the initial-state entropy. However, given this single piece of experimental data, and an assumed equation of state (usually a hybrid of the Landau EOS and a hadronic EOS, with a mixed phase), they are able to successfully calculate the effects of transverse pressure on particle spectra (radial flow) the mapping from the initial-state geometry to anisotropies in the final-state transverse momentum distributions (elliptic flow)[20].

Several clear signatures of radial flow are present in the experimental data even without recourse to particular models[14]. At low transverse momentum ($p_{\rm T} < m$) it is observed that the particle spectra harden with increasing particle mass. Elliptic flow has now been comprehensively described by calculations using boost-invariant hydrodynamics, both as a function of centrality and $p_{\rm T}$. A instance is shown in left panel of Fig. 4, which exhibits that the asymmetry parameter v_2 has a dependence of transverse momentum. Given the obvious discrepancy between the assumption of boost-invariance used in these calculations and the manifestly boost non-invariant particle distributions shown by the BRAHMS[1] data, it is not surprising to find that it is difficult to reproduce the dependence of v_2 on η as measured by PHOBOS[2],

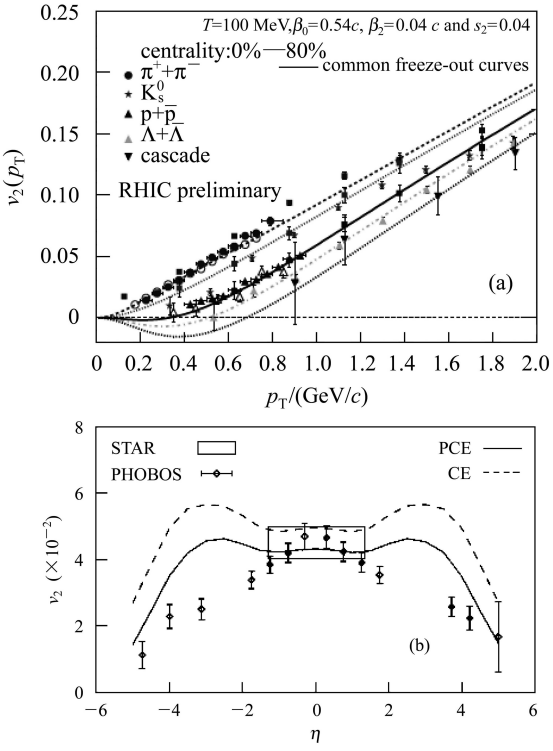

Fig. 4. (a) v_2 as a function of $p_{\rm T}$ for various particle species, compared to a hydrodynamics-inspired fit. (b) v_2 as a function of η compared with 3D hydro calculations.

as shown[23] in the right panel of Fig. 4. It shows that we need to understand the initial conditions in some detail.

In conclusion, we have found that the hydrodynamics approach is well consistent with a wide range of data, although no existing model or code can describe every detail correctly. This is especially true when considering longitudinal dynamics, which has not yet been fully incorporated into models that describe many features of the transverse dynamics[14].

2.2 Centrality

As mentioned above, we characterize centrality by number of participants $N_{\rm part}$ (∼volume) or number of binary collisions $N_{\rm coll}$. Once the choice of pseudorapidity region for the centrality determination is made and the corresponding efficiency is determined, the resulting multiplicity related distribution can be divided into percentile of total cross-section bins. Comprehensive MC simulations of these signals, that include Glauber model calculations of the collision geometry, allow the estimation of $N_{\rm part}$ for a cross section bin.

Shown[24] in the left panel of Fig. 5 is the ratio ν, which is the average number of binary nucleon-nucleon collisions every nucleon undergoes within a nucleus-nucleus collision, as a function of the $N_{\rm part}$. As this plot shows, a study of the centrality dependence of particle production allows a large variation of ν. The right panel in Fig. 5 shows[25] the measured $\mathrm{d}N_{\rm ch}/\mathrm{d}\eta$ distributions for charged particles for several different centrality ranges.

A similar parameter, typically denoted with $\bar{\nu}$ and calculated from $\bar{\nu}=(A\sigma_{\rm pp})/\sigma_{\rm pA}$ where the σ's are inelastic cross sections, is commonly used to characterize centrality or target dependence of observables in p-A collisions[26]. In nucleus-nucleus collisions, the calculated average number of collisions per participant varies by a large factor as a function of centrality and also has some dependence on energy due to the varying nucleon-nucleon cross section[2]. Centrality is typically parameterized by the number of participating nucleon pairs ($N_{\rm part}/2$), or the number of binary nucleon-nucleon collisions ($N_{\rm coll}$), in the overlapping region. Both quantities grow with the increasing centrality (decreasing impact parameter) of the collision.

2.3 Energy density

In ultra-relativistic heavy ion collisions, the maximum energy density occurs just as the two highly Lorentz contracted nuclei collide. In any reference frame, the more interesting quantity is the energy density carried by particles which are closer to equilibrium conditions. These conditions are roughly equivalent to restricting the particles to a range of

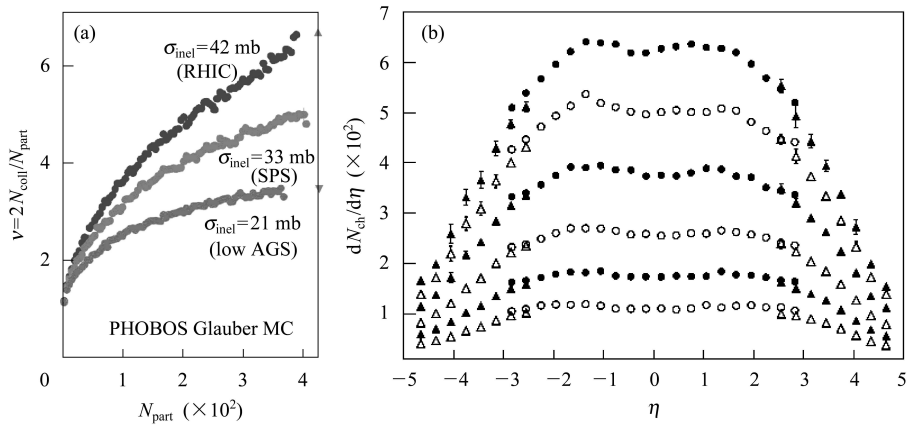

Fig. 5. (a) Ratio ν vs. $N_{\rm part}$ for inelastic process for RHIC, SPS and low alternating gradient synchrotron (AGS) experiments from PHOBOS Glauber MC. (b) Distributions of $\mathrm{d}N_{\rm ch}/\mathrm{d}\eta$ for centrality ranges of, top to bottom, 0%—5%, 5%—10%, 10%—20%, 20%—30%, 30%—40%, and 40%—50% in Au+Au collisions at $\sqrt{s_{\rm NN}}$ = 200 GeV.

pseudorapidity $|\eta|$ <1. Because there are no means to directly measure energy density, it must be inferred from the properties of the detected particles. PHOBOS data[2] have been used to investigate what range of initial energy densities is consistent with the observations. Studies of pseudorapidity and transverse momentum distributions, as well as elliptic flow, have been combined to constrain assumptions about the energy in the system and the time evolution of the volume from which the particles emanate.

As shown in Fig. 20, the produced particle densities are at their maximum near midrapidity and increase with both collision energy and centrality. It is notable that multiplicity measurements were initially obtained by PHOBOS and later confirmed by the other experiments at every new beam energy and species provided during the first three RHIC runs[2]. The right panel of Fig. 24 is a compilation of the evolution of the midrapidity charged particle density, $\mathrm{d}N_{\rm ch}/\mathrm{d}\eta_{|\eta|<1}$, per participating nucleon pair, $\langle N_{\rm part}/2\rangle$, as a function of collision energy.

Before attempting to make detailed estimates of the energy density, it is important to stress that the midrapidity particle density at the top RHIC energy is about a factor of two higher than the maximum value seen at the SPS[27] and there is evidence that the transverse energy per particle has not decreased[28, 29]. Thus, with little or no model dependence, it can be inferred that the energy density has increased by at least a factor of two from $\sqrt{s_{\rm NN}}$=17 to 200 GeV. In addition to the measured particle multiplicities, we must know the average energy per particle carried in order to estimate the energy density more precisely, as well as the volume from which they originate. PHOBOS data for the transverse momentum distribution of charged particles[30] can be used to find a mean transverse momentum. Fig. 6 compares the identified particle yields at very low transverse momentum measured by PHOBOS[31] and PHENIX data[32] for higher momenta.

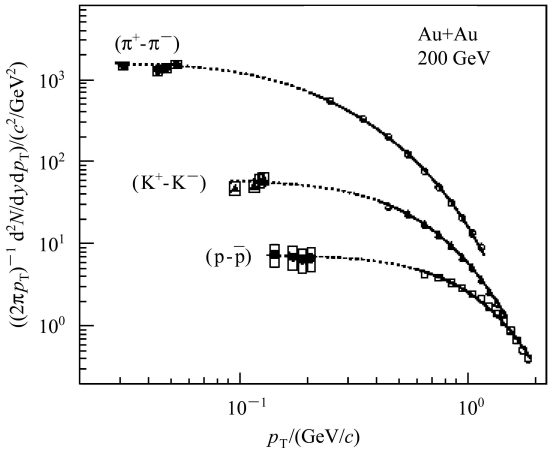

Fig. 6. Transverse momentum distributions of identified charged particles emitted near midrapidity in central Au+Au collisions at $\sqrt{s_{\rm NN}}$ = 200 GeV.

The low momentum identified particle data shown in Fig. 6 are in non-overlapping regions of $p_{\rm T}$ for the three different species. Accounting for the yields of the various particles, an average transverse momentum for all charged particles of $\langle p_{\rm T}\rangle \approx$500 MeV/$c$ can be derived. Averaging over the pions, kaons, and nucleons, and assuming the yields for the unobserved neutral particles, an average transverse mass, $m_{\rm T}$, of $\approx$570 MeV/c^2 can be extracted.

The total energy in the system created near midrapidity in central Au+Au collisions at $\sqrt{s_{\rm NN}}$ = 200 GeV can be found from[2]

$$E_{\rm tot} = 2E_{\rm part}\mathrm{d}N_{\rm ch}/\mathrm{d}\eta_{|\eta|\leqslant 1} f_{\rm neut} f_{4\pi}\,. \qquad (1)$$

where $E_{\rm part}$ is the average energy per particle,

$dN_{ch}/d\eta_{|\eta|\leqslant 1}$=655±35 (system) is the midrapidity charged particle density for the 6% most central collisions, f_{neut} is a factor of 1.6 to roughly account for the undetected neutral particles, and the factor of 2 integrates over $-1 \leqslant \eta \leqslant 1$. The correction for these additional particles, $f_{4\pi}$, is trivially estimated from the fraction of solid angle outside θ=40°—140°. (i.e., outside $|\eta| \leqslant 1$) and equals about 1.3. It should be stressed that this methodology does not suggest that the entire distribution of particles is isotropic. Instead, the goal is to obtain the energy density for the component of the distribution which is consistent with the isotropic emission from a source at midrapidity. Combining all of these terms, the total energy contained in all particles emitted near midrapidity, with transverse and longitudinal momenta consistent with emission from an equilibrated source, is about 1600 GeV.

The next thing we should know is the volume within which this energy is contained at the earliest time of approximate equilibration. For central collisions, a transverse area equal to that of the Au nuclei (≈150 fm^2) can be assumed, but which value to use for the longitudinal extent is not as clear. One extreme[2] is to take the very first instant when the two Lorentz contracted nuclei overlap (longitudinal size ≈0.1 fm), which yields an upper limit on the energy density in excess of 100 GeV/fm^3. There is, however, no reason to assume that at such an early instant the system is in any way close to equilibrium. A second commonly-used assumption is that proposed by Bjorken[21], namely, a transverse size equal to the colliding nuclei and a longitudinal size of 2 fm (corresponding to a time of the order of $\tau \approx 1$ fm/c since the collision) which implies an energy density of about 5 GeV/fm^3. This estimate is much higher than the energy density inside nucleons.

2.4 Degree of nuclear stopping

Through baryon stopping mechanism we can get that it defines available energy for particle production. The independence of the forward and backward hemispheres (hadronic factorization) suggests a picture of hadronic interactions where the net baryon distribution is built up from two components: one connected to the target and the other to the projectile[33]. In Fig. 7 this projectile component is presented[34].

With increasing centrality, the projectile component of the net proton distribution has a similar behavior in p-A and A+A interactions, demonstrated in Fig. 7, exhibiting a smooth transition of baryon number transfer from the elementary to the more complex nuclear interactions. But for p-p interactions the x_F distribution is flat and has about 50% energy loss.

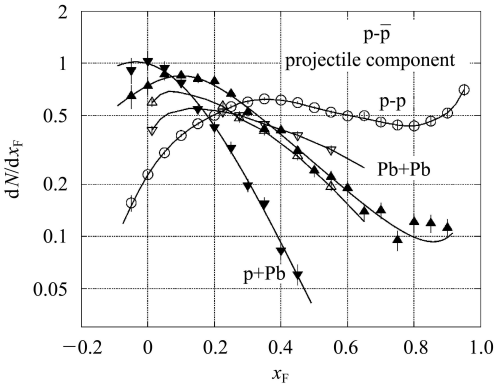

Fig. 7. The projectile component of the net proton distribution in elementary and nuclear interactions for two centralities.

Baryon stopping for central collisions at ultrarelativistic energies increases with system size. The integrated yield and rapidity density of negative hadrons exhibit scaling with the number of participant nucleons for nuclear collisions, and a small enhancement with respect to A+A collisions[35], as shown in Fig. 8.

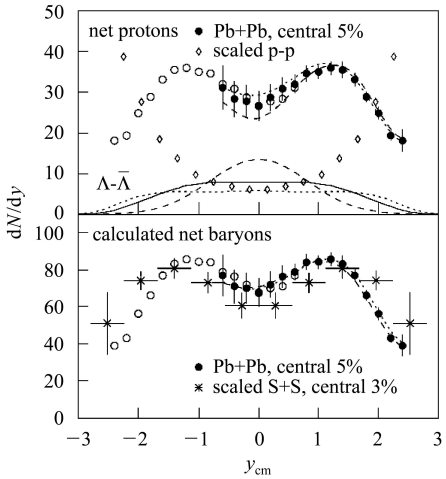

Fig. 8. **Upper**: The normalized rapidity distributions of p-p̄ for Pb+Pb collisions. Also shown are the corresponding Λ-Λ̄ rapidity distributions, and the scaled proton distribution for p-p collisions. **Lower**: The normalized rapidity distributions of $N_B - N_{\bar{B}}$ from Equation $N_B - N_{\bar{B}} = (2.07\pm0.05)\cdot(N_p - N_{\bar{p}}) + (1.6\pm0.1)\cdot(N_\Lambda - N_{\bar{\Lambda}})$ for Pb+Pb, and scaled $N_B - N_{\bar{B}}$ for S+S.

Baryon number is conserved, and rapidity distributions are only slightly affected by rescattering in late stages of the collision, the measured net-baryon $(B-\bar{B})$ distribution retains information about the energy loss and allows the degree of nuclear stopping to be determined[36]. Such measurements can also distinguish between different proposed phenomenological mechanisms of initial coherent multiple interactions and baryon transport[37—39]. Bjorken assumed

that sufficiently high energy collisions are "transparent", thus the midrapidity region is approximately net-baryon free[21].

Figure 9 shows net-proton dN/dy measured at AGS and SPS compared with these results[36]. The net-proton distribution shows that collisions at RHIC energies are quite transparent compared with lower energies.

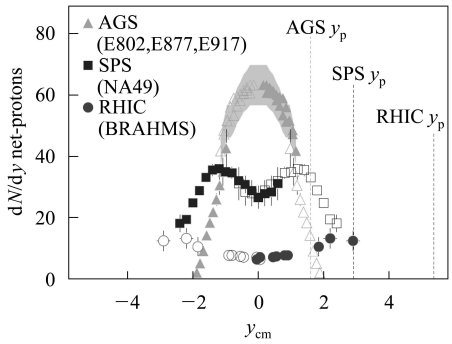

Fig. 9. The net-proton rapidity distribution at AGS (Au+Au at $\sqrt{s_{NN}}$ = 5 GeV), SPS[35] (Pb+Pb at $\sqrt{s_{NN}}$ = 17 GeV) and this measurement ($\sqrt{s_{NN}}$ = 200 GeV).

Figure 10 the inserted plot shows the extrapolated net-baryon distribution (data points) with fits (represented by the curves) to the data[36]. The full figure shows the rapidity loss as a function of projectile rapidity (in the Center-of-Mass). By extrapolation to the full net-baryon distribution, we find that the rapidity loss scaling observed at lower energy is broken and the rapidity loss seems to saturate between SPS and RHIC energies.

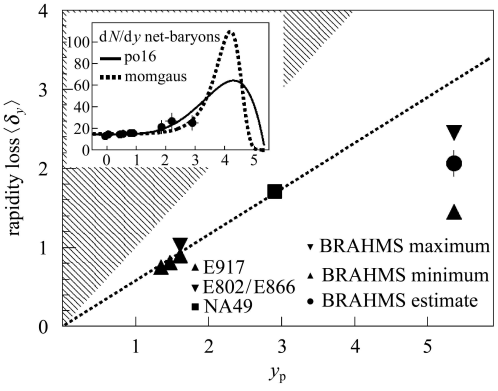

Fig. 10. (insert) The net-baryon dN/dy obtained from the measured net-proton dN/dy. (Full) The rapidity loss.

2.5 Limiting fragmentation

In order to understand the relation between particle production and collision mechanisms, we consider particle production away from mid-rapidity in the target (or projectile) rest frame. The $\eta'=\eta-y_{\rm beam}$ variable is used. It is measurable without particle identification and approximately transforms the distributions to the rest frame of one of the colliding particles/ions. The rapidity, y, is defined as $y=0.5\ln\dfrac{E+p_z}{E-p_z}$. Rapidity variables are in the center-of-mass system with $y_{\rm p}$ positive. The pseudorapidity variable η is related to the particle emission angle θ with $\eta=-\ln[\tan\theta/2]$.

In proton-proton collisions, the so-called limiting fragmentation[40] is seen from a few GeV to 900 GeV collision energy (e.g. at CDF, UA5 and ISR). The left panel of Fig. 11[41] shows that the charged particle pseudorapidity density distributions are approximately independent of collision energy over a large range of η', which grows with $\sqrt{s}$. The same phenomenon is observed in e$^+$-e$^-$ collisions, as shown in the right panel of Fig. 11[42].

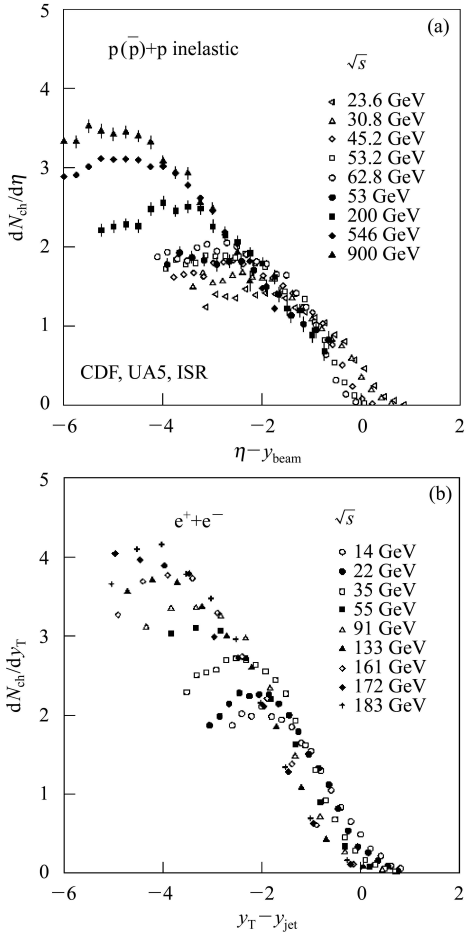

Fig. 11. (a) Pseudorapidity density distributions of charged particles emitted in p($\bar{\rm p}$)-p collisions at various energies[43—45]. (b) Similar data for particles emitted along the jet axis in an e$^+$-e$^-$ collision versus the variable $y_{\rm T}$-$y_{\rm jet}$[46].

As Fig. 12 showed[41], similar scaling was observed for p-A collisions between $\sqrt{s_{\rm NN}}$=6.7 and 38.7 GeV, and more recently in d-Au collisions at $\sqrt{s_{\rm NN}}$ = 200 GeV[47, 48]. The observed energy-independence of these distributions holds both for the projectile and for the target reference frames[47].

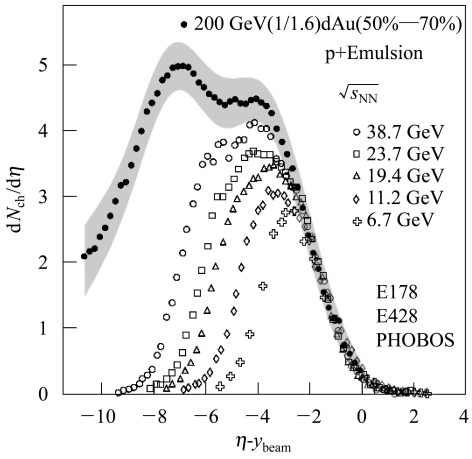

Fig. 12. Pseudorapidity density distributions of charged particles emitted in d-Au, p-emulsion collisions at various energies.

The data from PHOBOS show a number of interesting features, as shown in Fig. 13 and Fig. 14[49].

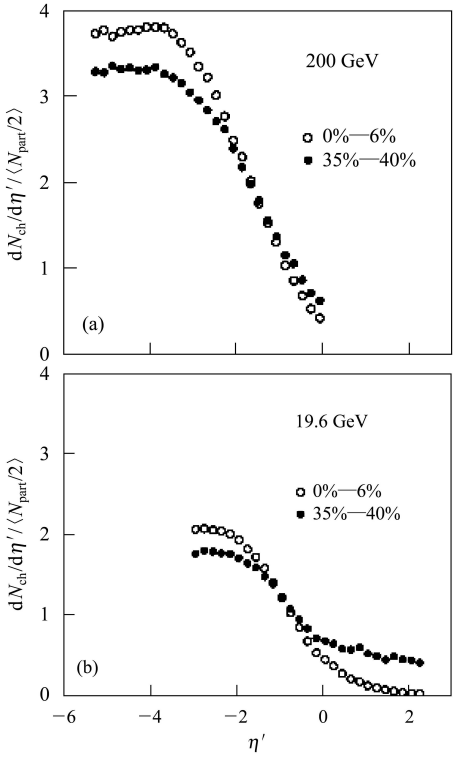

Fig. 13. The distribution $\mathrm{d}N_{\rm ch}/\mathrm{d}\eta'$ per participant pair for central (0%—6%) and noncentral (35%—40%) Au+Au collisions for (a) $\sqrt{s_{\rm NN}}$ = 200 GeV and (b) $\sqrt{s_{\rm NN}}$ = 19.6 GeV.

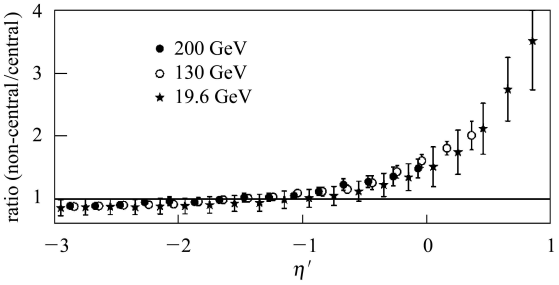

Fig. 14. The ratio of $\mathrm{d}N_{\rm ch}/\mathrm{d}\eta'$ per participant pair between central (0%—6%) and noncentral (35%—40%) data plotted for $\sqrt{s_{\rm NN}}$=200, 130, and 19.6 GeV.

First, limiting fragmentation (energy independence of $\mathrm{d}N/\mathrm{d}\eta'$) is valid over a large range of η'. Second, the scaled $\mathrm{d}N/\mathrm{d}\eta$ shape is not independent of centrality at high η. The η distribution is broader in peripheral collisions than in central collisions. Third, as in p-$\bar{\rm p}$ collisions, the fragmentation region in Au+Au collisions grows in pseudorapidity extent with beam energy, which is becoming a dominant feature of the pseudorapidity distributions at high energy.

2.6 Leading particle effect

In hadron-hadron and lepton-hadron interactions, a well-known feature is that one particular particle in the final state often has a momentum close to the maximum permitted. This observation is commonly referred to as the "leading particle effect", and it has been related to the quantum number flow from the initial state to the particle in the final state, on the basis that the particle which carries more constituents of the initial state will have a sizable fraction of the four-momentum of the initial state[50].

The PHOBOS experiment has demonstrated two kinds of universal behavior are observed in charged particle production in heavy ion collisions at three RHIC energies[51]. One is that forward particle production follows a universal limiting curve with a nontrivial centrality dependence over a range of energies. The other arises from comparisons with pp/$\bar{\rm p}$p and $\mathrm{e^+e^-}$ data, $\langle N_{\rm ch}\rangle/\langle N_{\rm part}/2\rangle$ in nuclear collisions at high energy scales with $\sqrt{s}$ in a similar way as $N_{\rm ch}$ in $\mathrm{e^+e^-}$ collisions and has a very weak centrality dependence.

As shown of Fig. 15(a), the comparisons can be seen more clearly by dividing all of the data by a fit to the $\mathrm{e^+e^-}$ data, seen in Fig. 15(b). The pp/$\bar{\rm p}$p data follows the same trend as $\mathrm{e^+e^-}$, but it can be shown that it matches very well if the "effective energy" $\sqrt{s_{\rm eff}} = \sqrt{s}/2$ is used, which accounts for the leading particle effect seen in pp collisions[52, 53].

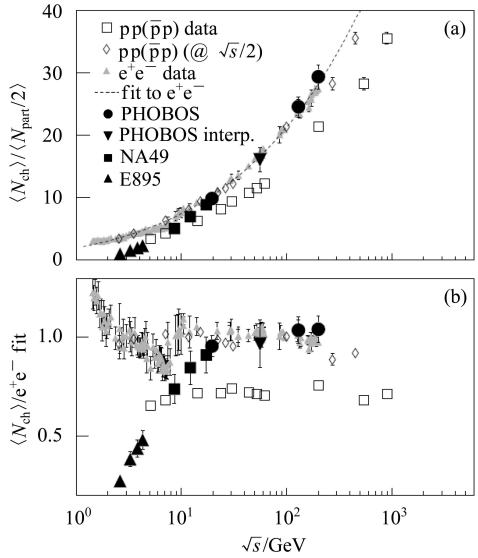

Fig. 15. Comparison of $\langle N_{\rm ch}\rangle/\langle N_{\rm part}/2\rangle$ for A+A, pp/$\bar{\rm p}$p (a) and $\rm e^+e^-$ data compared with a fit to the $\rm e^+e^-$ data (b).

This feature may be related to a reduction in the leading particle effect due to the multiple collisions suffered per participant. In this situation, the Au+Au data suggest a reduced leading particle effect in central collisions of heavy ion at high energy. The yield of high transverse momentum ($p_{\rm T}\gtrsim$5 GeV/c) leading particle in Au+Au collisions at the top RHIC energy, $\sqrt{s_{\rm NN}}$ = 200 GeV, is suppressed by a factor of about five lower than expected from the measurements in p-p collisions at the same energy[54, 55]. The absence of this effect in d-Au collisions at the same energy supports the partonic energy loss scenario[56].

The leading-particle suppression is usually quantified by the nuclear modification factor,

$$R_{\rm AA}(p_{\rm T},\eta)=\frac{1}{\langle N_{\rm coll}\rangle_{\rm centrality\ class}}\times\frac{{\rm d}^2N_{\rm AA}/{\rm d}p_{\rm T}{\rm d}\eta}{{\rm d}^2N_{\rm pp}/{\rm d}p_{\rm T}{\rm d}\eta}\,. \tag{2}$$

as the ratio of the yield in A+A over the binary-scaled yield in pp for a given centrality class. At mid-rapidity, in Au+Au collisions at $\sqrt{s_{\rm NN}}$ = 200 GeV, $R_{\rm AA}$ is found to decrease from the peripheral ($R_{\rm AA}\simeq$1) to the central events ($R_{\rm AA}\simeq$0.2), for $p_{\rm T}\gtrsim$5 GeV/c (see Fig. 16).

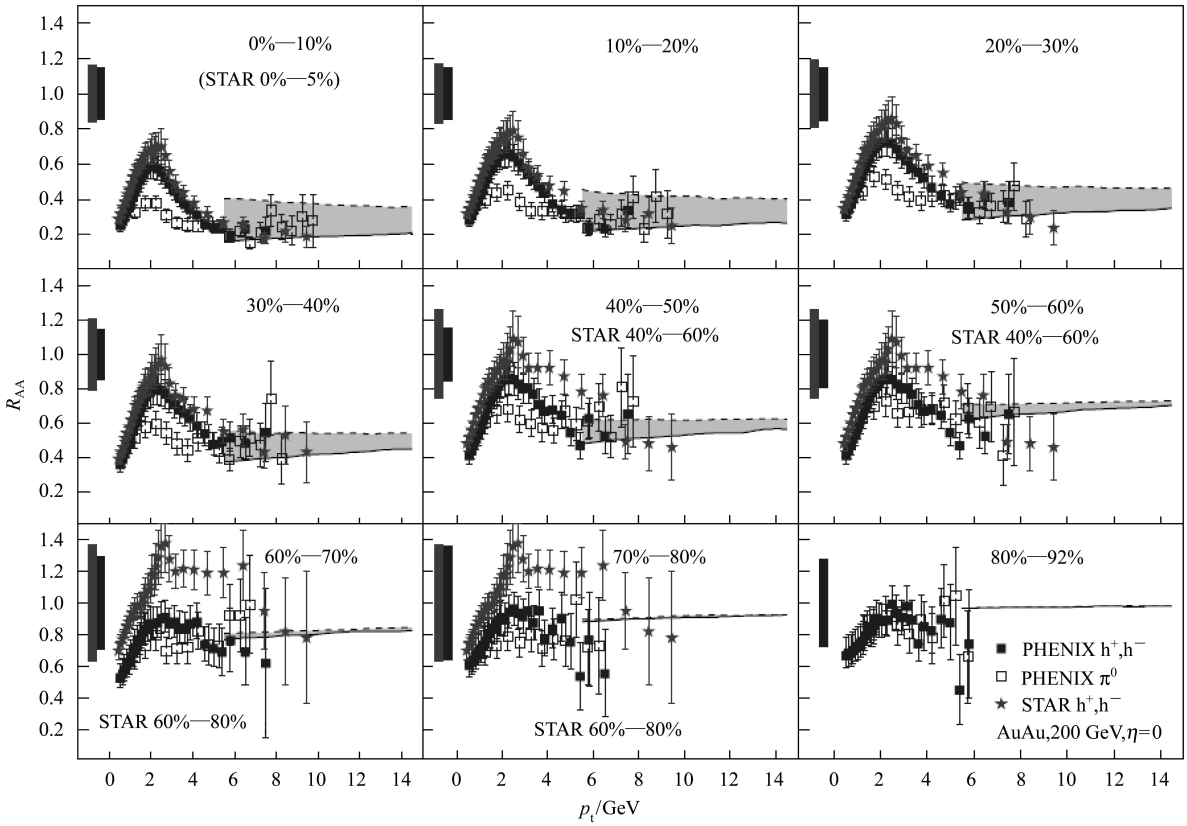

Fig. 16. $R_{\rm AA}(p_{\rm T})$ in Au+Au collisions at $\sqrt{s_{\rm NN}}$ = 200 GeV for different centralities.

3 Particle production

3.1 Rapidity distribution

As the definitions for rapidity y and pseudorapidity η, we use rapidity distribution to describe the longitudinal phase space, and consider the pseudorapidity equal to the rapidity approximately. We can describe the relations between the rapidity and the pseudorapidity by Eq. (3).

$$\frac{{\rm d}N}{{\rm d}\eta{\rm d}p_{\rm T}}=\beta\frac{{\rm d}N}{{\rm d}y{\rm d}p_{\rm T}}\,. \tag{3}$$

where the parameter β indicates a discrepancy between η and y. We generally set β to 1.1 in calculations.

Pseudo-rapidity distributions in p-p collisions are shown[57] in Fig. 17. The pseudorapidity distributions of charged particles with HIJING model are in good agreement with the energy dependence of the collider data[43, 58].

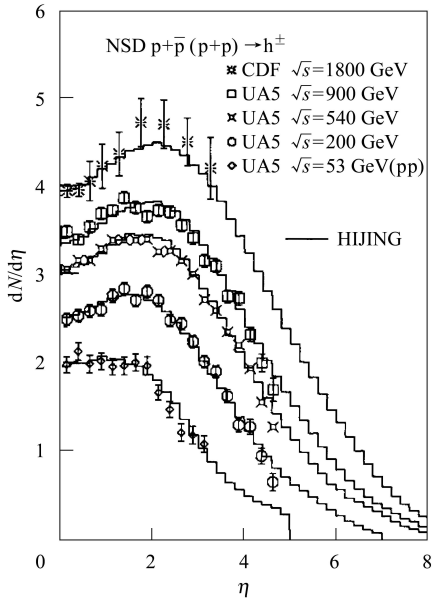

Fig. 17. Pseudorapidity distributions of charged particles in non-single-diffractive pp at $\sqrt{s_{\rm NN}}$ = 53 GeV, p-$\bar{\rm p}$ collisions at $\sqrt{s_{\rm NN}}$ = 200, 540, 900 and 1800 GeV.

Pseudorapidity densities of charged particles for the d-Au reaction at $\sqrt{s_{\rm NN}}$ = 200 GeV are presented for different centrality ranges. The ratio of particle densities for the central and the peripheral events is found to agree well with the participant scaling in terms of the respective fragments away from midrapidity, seen in Fig. 18. Overall, model calculations based on both soft physics and perturbative QCD (HIJING, AMPT) lead to excellent agreement with the experimental results. Calculations based on the saturation picture using scale parameters set by previous experimental data fail to reproduce the measurements and lead to a pseudorapidity dependence very different from that observed with the current data[48].

Pseudorapidity distributions in d-Au collisions are shown in Fig. 18[48] and Fig. 19[47], respectively.

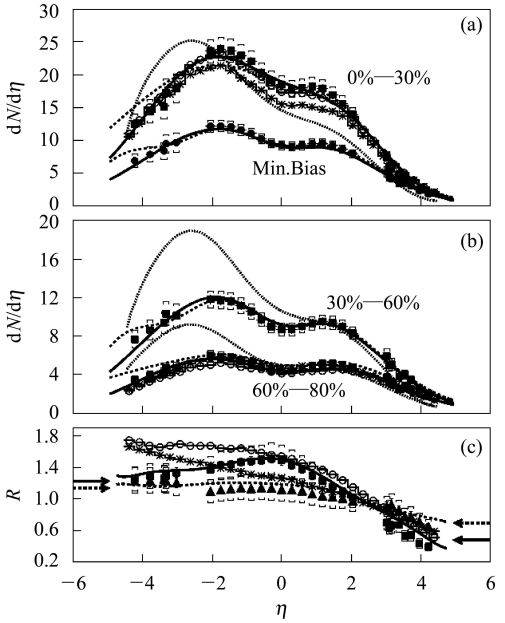

Fig. 18. (a),(b) Charged-particle pseudorapidity densities for indicated centrality ranges. (c) Multiplicity ratios $R^{0—30}$ (squares) and $R^{30—60}$ (triangles).

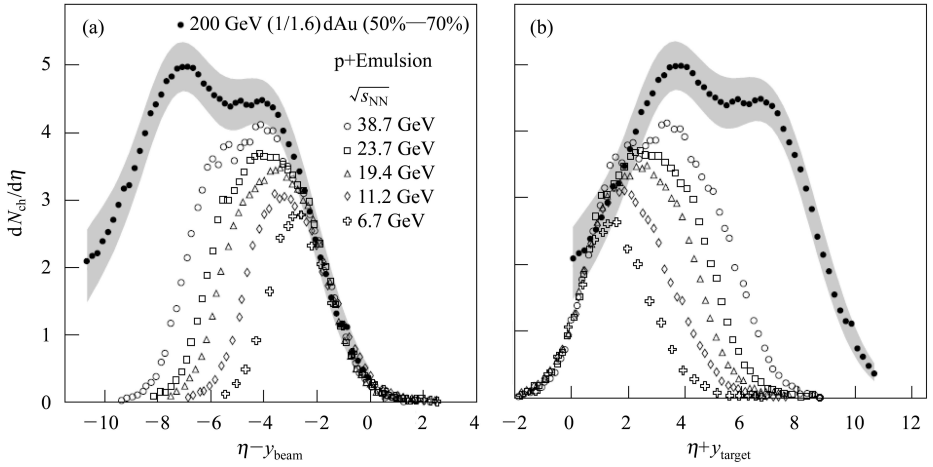

Fig. 19. Comparison of d$N_{\rm ch}$/dη distributions for d+Au collisions at $\sqrt{s_{\rm NN}}$ = 200 GeV to p+Em collisions (sum of shower and gray tracks) at five energies with η shifted to $\eta - y_{\rm beam}$ (a) and $\eta + y_{\rm target}$ (b).

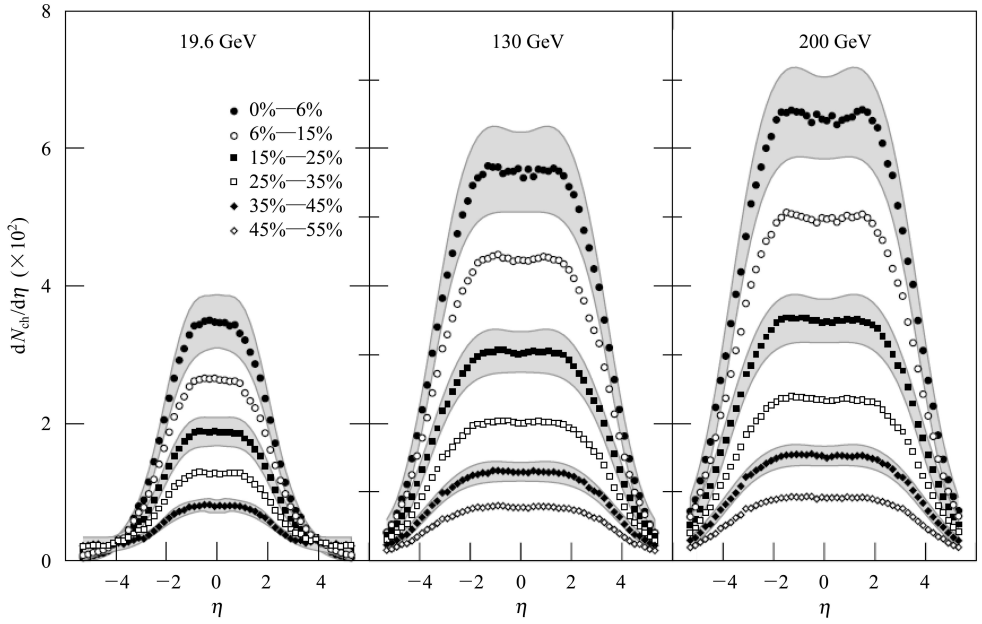

Fig. 20. $\mathrm{d}N_{\mathrm{ch}}/\mathrm{d}\eta$ vs η (solid and open points) for five centrality bins representing 45% of the total cross section for $\sqrt{s_{\mathrm{NN}}}$ = 19.6 GeV Au+Au collisions and for six centrality bins for $\sqrt{s_{\mathrm{NN}}}$=130 and 200 GeV corresponding to 55% of the cross section[49].

In Fig. 19, the η measured in the center-of-mass system has been shifted to $\eta - y_{\mathrm{beam}}$ in order to study the fragmentation regions in the deuteron/proton rest frame. Similar to this, but η ha been shifted to $\eta + y_{\mathrm{target}}$ in order to study the fragmentation regions in the gold/emulsion rest frame. From all above, we can find the longitudinal features of d-Au collisions at $\sqrt{s_{\mathrm{NN}}} = 200$ GeV, as reflected by the centrality dependence of the pseudorapidity distributions of charged particles, are very similar to those seen in p-A collisions at energies lower by more than an order of magnitude.

Pseudorapidity distributions in Au+Au collisions are shown in Fig. 20[49]. From the figure, we can find that for central collisions at the highest energy, we find that a total of more than 5000 charged particles are produced. These results span 11 units of pseudorapidity, a factor of 10 in energy, and a factor of 5 in $\langle N_{\mathrm{part}} \rangle$-all measured in a single detector.

While the scaled multiplicities increase with centrality at midrapidity, Fig. 21[25] shows they are independent of both the collision centrality and the beam energy over a pseudorapidity range from 0.5 to 1.5 units below the beam rapidity.

This is found for energies ranging from the CERN/SPS energy ($\sqrt{s_{\mathrm{NN}}}$ = 17 GeV)[59] to the present RHIC beam energy and is consistent with a limiting-fragmentation picture in which the excitations of the fragment baryons saturate at a moderate collision energy, independent of system size[60]. The increased projectile kinetic energy is utilized for particle production below beam rapidity, as evidenced by the observed increase in the scaled multiplicity for central events at midrapidity.

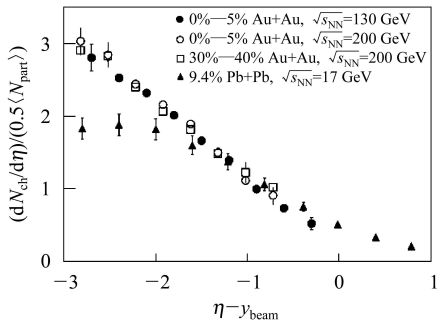

Fig. 21. Charged-particle multiplicities normalized to the N_{part} pairs for the Pb+Pb data[59] and the Au+Au results[60].

3.2 Angular distribution

Some of the general properties of charged particle multiplicity distributions[61] may be seen in Fig. 22. Panel a: The pseudorapidity density, $\mathrm{d}N/\mathrm{d}\eta$ is shown as a function of η. Panel b: The corresponding angular distribution $\mathrm{d}N/\mathrm{d}\theta$ is shown as a function of the angle θ relative to the beam axis. Panel c: the same as for panel (b) but here $\mathrm{d}N/\mathrm{d}\Omega$ is shown. The shaded regions in panels (a) and (b) indicate the angular region where the transverse momentum p_{T} exceeds the longitudinal momentum $p_{||}$.

Since the particles emitted within the angular region $45^\circ < \theta < 135^\circ$ corresponding to $-0.88 < \eta < 0.88$ (grey bands in panels (a) and (b)) are most likely to represent a thermalized region of phase space, there is a special significance attached to the number of

charged particles emitted in this region, i.e. the height of the mid-rapidity plateau or $\mathrm{d}N_{\mathrm{ch}}(|\eta|<1)/\mathrm{d}\eta$. Although this region appears as a plateau in the $\mathrm{d}N_{\mathrm{ch}}/\mathrm{d}\eta$-distribution shown in Panel (a) it is interesting to observe that the $\mathrm{d}N_{\mathrm{ch}}/\mathrm{d}\theta$ and the $\mathrm{d}N_{\mathrm{ch}}/\mathrm{d}\Omega$ distributions both exhibit a minimum at θ=90° corresponding to η=0. As shown in Fig. 22, there are only 22% of the total emitted charged particles with $p_{\mathrm{T}} > p_{||}$, however, these particles carry information about the densest region form in the collisions.

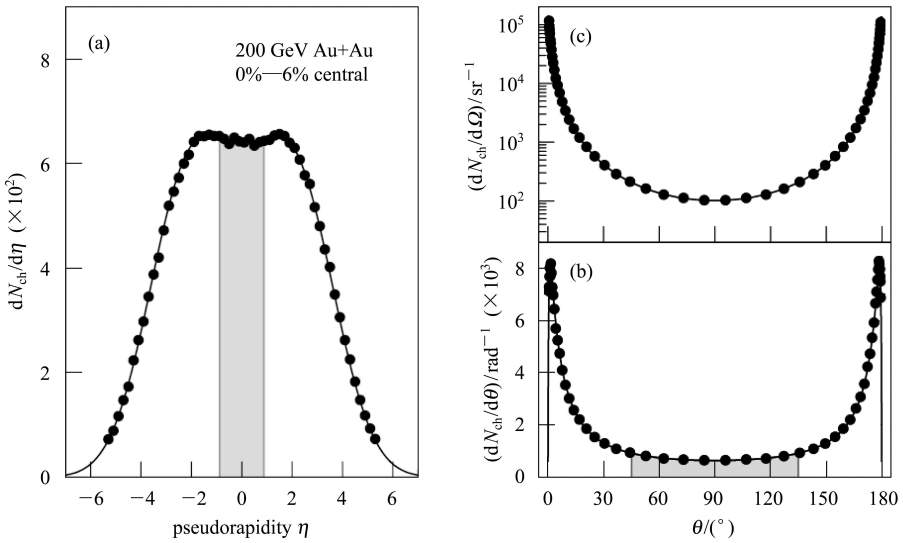

Fig. 22. Illustration charged particle distribution for 0%—6% central 200 GeV Au+Au collisions.

3.3 Multiplicity distribution

In Fig. 23 we show the normalized yield per participant obtained for Au+Au collisions, proton-antiproton (p-$\bar{\mathrm{p}}$) collisions[43] and central Pb+Pb collisions at the CERN/SPS.

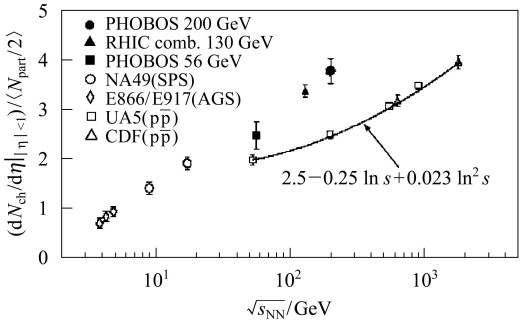

Fig. 23. Measured pseudorapidity density normalized per participant pair for central Au+Au collisions[43, 62].

Several important features of the data emerge: First, the central Au+Au collisions show a significantly larger charged particle density per participant than for example non-single diffractive (NSD) p-$\bar{\mathrm{p}}$ collisions at comparable energies. This rules out simple superposition models such as the wounded nucleon model[63] and is compatible with the predictions of models like HIJING that include particle production via hard-scattering processes. Secondly, the observed increase by 31% from 56 to 130 AGeV in central Au+Au collisions is significantly steeper than the increase shown by a p-$\bar{\mathrm{p}}$ parametrization (see Fig. 23) for the same energy interval[43]. Finally, comparing the RHIC data with those obtained at the CERN/SPS for Pb+Pb collisions at $\sqrt{s}=17.8$ AGeV, we find a 70% higher particle density per participant near η=0 at $\sqrt{s}$=130 AGeV. General arguments suggest that this increase should correspond to a similar increase in the maximal energy density achieved in the collision.

Several theoretical predictions had been made concerning the density of charged particles at mid-rapidity for $\sqrt{s_{\mathrm{NN}}}$ = 200 GeV central Au+Au collisions, shown in the left panel of Fig. 24[2]. It is evident that most of the predictions overestimated the density by up to a factor of two although a few predictions agree with the measurements.

Among the models which predicted a value close to that seen in the data were two which invoked the concept of saturation in either the initial state or the produced partons. However, the search for other evidence for possible parton saturation effects remains a topic of interest at RHIC. The dependence on collision energy is shown in the right panel of Fig. 24[2].

The PHENIX results for N_{ch} are compared with the data available from the other RHIC experiments[65]. This comparison is shown in the left panels of Fig. 25.

There is good agreement between the results of BRAHMS[25, 60], PHENIX, PHOBOS[62, 66, 67], and STAR[68, 69] using N_{part} based on a Monte Carlo-Glauber model. This agreement is very impressive because all four experiments use different apparatuses

and techniques to measure the charged particle production. The systematic errors of all results are uncorrelated, except for those related to the same Glauber model, which are small. That makes it possible to calculate the RHIC average and reduce the systematic uncertainty. The averaged results from all four RHIC experiments are plotted in the right panel of Fig. 25.

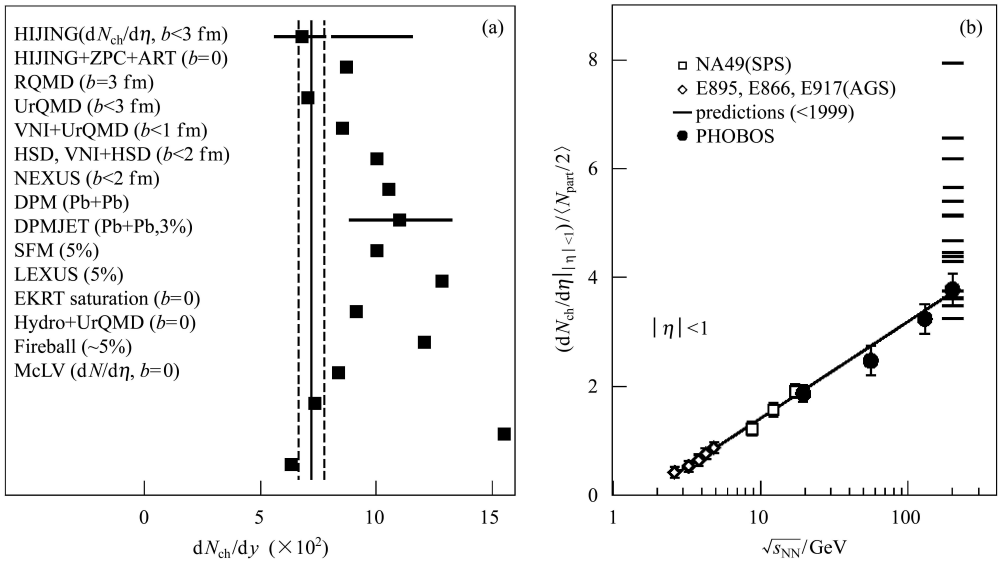

Fig. 24. (a) A compilation of theoretical model predictions (solid squares) of the midrapidity density of charged particles $dN_{ch}/d\eta$ or dN_{ch}/dy[64]. (b) The energy dependence of the pseudorapidity density at $|\eta| < 1$.

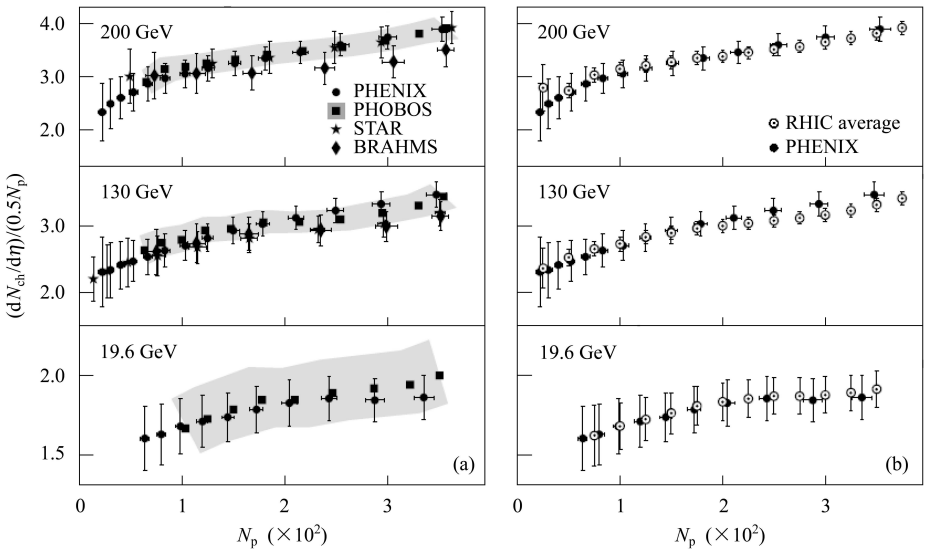

Fig. 25. (a) $dN_{ch}/d\eta$ per pair of N_{part} measured by the four RHIC experiments at different energies. (b) RHIC average values (including PHENIX) compared to the PHENIX results.

It should be pointed out that the universal N_{part} scaling of the total number of particles produced in Au+Au collisions does not result from rapidity distributions whose shape is independent of centrality, or N_{part}. The rapidity distributions do depend on both centrality and on the nature of the colliding systems, as is evident from Fig. 26[2] for Au+Au collisions[49]. The data have been divided by the average number of pairs of participating nucleons for each energy and centrality range.

Comparison of the total charged-particle multiplicity in RHIC with e^+e^- and $pp/p\bar{p}$ data is shown as Fig. 27[17].

Figure 27(a) shows the shapes of Au+Au and e^+e^- are similar (within 10%) in shape and magnitude, especially within $|\eta|$ <4. It is observed that the Au+Au data are very similar in magnitude and shape to the e^+e^- data at the same $\sqrt{s}$, and similar

in shape to the pp data (as shown in Fig. 27(b)), over a large range in η. The differences between the e^+e^- and Au+Au distributions shown in Fig. 27(a) can be partly attributed to the different kinematic variables.

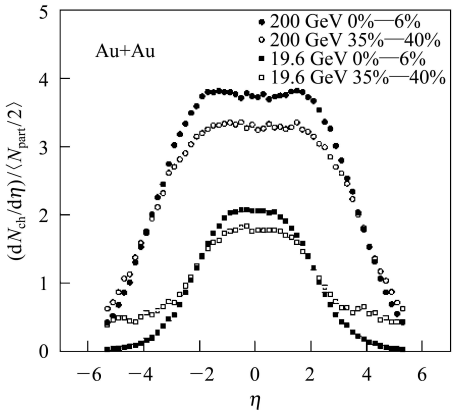

Fig. 26. Distributions of normalized pseudorapidity densities of charged particles emitted in Au+Au collisions at two energies and two ranges of centrality.

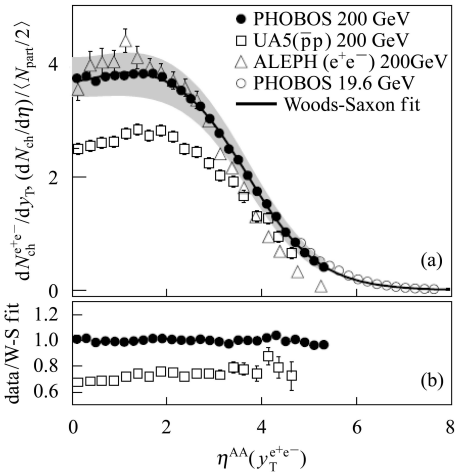

Fig. 27. (a) $dN_{ch}/d\eta/\langle N_{part}/2\rangle$ for central Au+Au collisions at $\sqrt{s_{NN}} = 200$ GeV compared with pp and e^+e^- data. (b) Au+Au and p-p data divided by a fit to the Au+Au data.

Multiplicity and pseudorapidity distributions of photons in Au+Au collisions at $\sqrt{s_{NN}} = 62.4$ GeV[70] is shown as Fig. 28 and Fig. 29. Fig. 28 shows the N_γ per N_{part} pair is approximately constant with centrality. Approximate linear scaling of N_γ with N_{part} in the η range studied indicates that photon production is consistent with the nucleus-nucleus collisions being a superposition of nucleon-nucleon collisions.

We observe in Fig. 29(a) that photon results from the SPS and RHIC are consistent with each other, suggesting that photon production follows an energy independent LF (Limiting Fragmentation) behavior, and also observe that $dN_\gamma/d\eta$ as a function of $\eta - y_{beam}$ is independent of centrality. Energy independent LF behavior for charged particles can be seen in Fig. 29(b). It also indicates that there is apparently an important charged baryon contribution in nucleus-nucleus collisions at the forward η region.

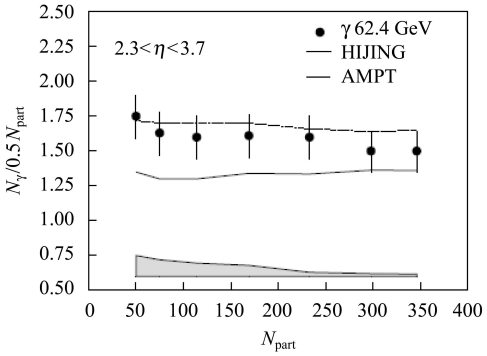

Fig. 28. Variation of N_γ per participant pair in $2.3 \leqslant \eta \leqslant 3.7$ versus N_{part}. The lower band reflects uncertainties in N_{part} calculations.

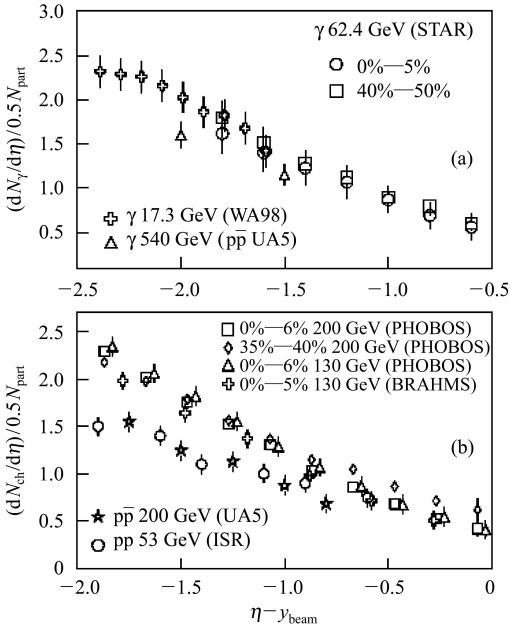

Fig. 29. (a) Variation of $dN_\gamma/d\eta$ normalized to N_{part} with $\eta - y_{beam}$ for different collision energy and centrality. (b) same as (a) for charged particles.

At midrapidity the charged particle multiplicities have been measured for Au+Au collisions as a function of both energy and centrality of the collisions. A surprising result is that the dependence on these two variables can be factorized to high accuracy ($\sim 1\%$)[71], as shown in Fig. 30.

3.4 Scaling behavior

Scaling of charged particle production in d-Au collisions at $\sqrt{s_{NN}} = 200$ GeV[47] is shown in Fig. 31 and

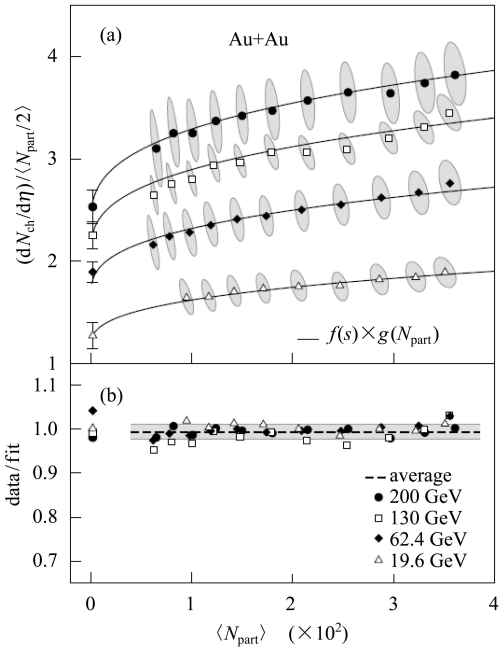

Fig. 30. (a) The pseudorapidity density, $dN/d\eta$ at $|\eta|<1$ is shown as a function of $N_{\rm part}$ for Au+Au and pp/p$\bar{\rm p}$ collisions. (b) The ratio of the data to the fit function $f(s)\times g(N_{\rm part})$ is seen to lie in a narrow band around unity.

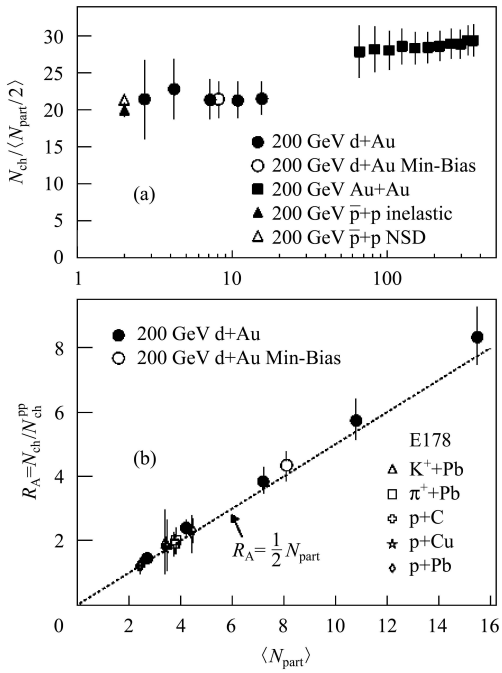

Fig. 31. Panel (a): Total integrated charged particle multiplicity per participant pair in d-Au, Au+Au[17], p($\bar{\rm p}$)-p inelastic[72, 73] and p($\bar{\rm p}$)-p NSD[74] collisions at $\sqrt{s_{\rm NN}}=200$ GeV. Panel (b): The ratio $R_{\rm A}=N_{\rm ch}/N_{\rm ch}^{\rm pp}$, where $N_{\rm ch}^{\rm pp}$ is the total number of charged particles for inelastic p($\bar{\rm p}$)-p collisions, as a function of $\langle N_{\rm part}\rangle$ for different collision systems.

Fig. 32. We find that in d-Au collisions the total multiplicity of charged particles scales linearly with the total number of participants, that the transition between the multiplicity per participant in d-Au and Au+Au collisions is not controlled simply by the total number of participants, and that the energy dependence of the density of charged particles produced in the fragmentation regions exhibits extensive longitudinal scaling.

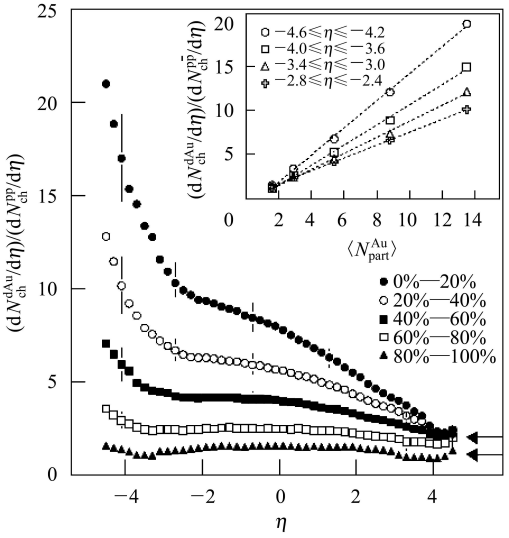

Fig. 32. Centrality dependence of the $dN_{\rm ch}/d\eta$ ratio of d-Au collisions relative to that for inelastic p($\bar{\rm p}$)-p collisions[58] at the same energy.

PHOBOS has measured the charged particle pseudorapidity density at midrapidity ($|\eta|<1$) for Au+Au collisions at energies of $\sqrt{s_{\rm NN}}=19.6$ and 200 GeV[75].

As shown in Fig. 33, we find an increase in particle production per participant pair for Au+Au collisions compared with the corresponding inelastic p($\bar{\rm p}$)-p values for both energies. The ratio of the measured yields at 200 and 19.6 GeV shows a clear geometry scaling over the central 40% inelastic cross section and averages to $R_{200/19.6}=2.03\pm0.02({\rm stat})\pm0.05({\rm syst})$.

In Cu+Cu and Au+Au collisions at the same collision energy, the charged hadron $dN/d\eta$ distributions are nearly identical in broad pseudorapidity range with the same $N_{\rm part}$, as shown in the left panel of Fig. 34[76]. Meanwhile, the increase in particle production per participant with increasing $N_{\rm part}$ is independent of collision energy over the full energy range of RHIC from 19.6 to 200 GeV, as shown in the right panel of Fig. 34[76].

3.5 Transverse momentum distribution

Transverse momentum distributions are one of the most common tools used in studying high energy collisions. This is because the transverse motion is generated during the collision and hence is sensitive to the dynamics[8]. The yield of charged hadrons produced in collisions of gold nuclei at an energy of

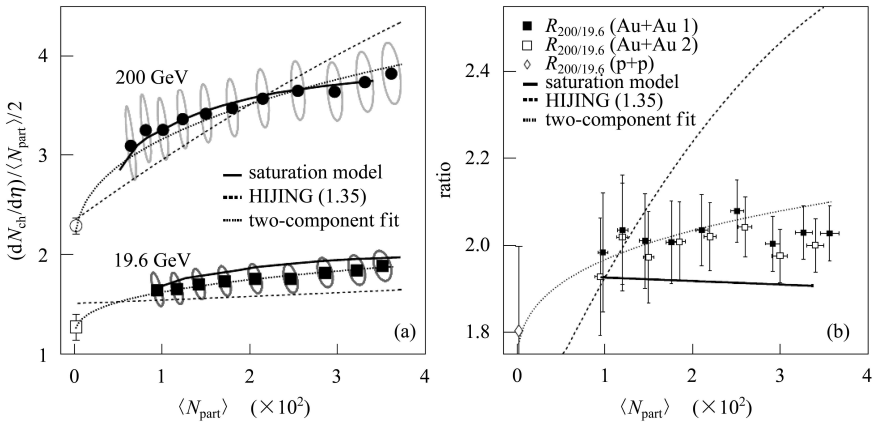

Fig. 33. (a) The measured pseudorapidity density per participant pair as a function of $\langle N_{\rm part}\rangle$ for Au+Au collisions at $\sqrt{s_{\rm NN}}$ = 19.6 GeV (closed squares), 200 GeV (closed circles). (b) The ratio, $R_{200/19.6}$, of the midrapidity pseudorapidity density per participant pair at 200 and 19.6 GeV versus $\langle N_{\rm part}\rangle$.

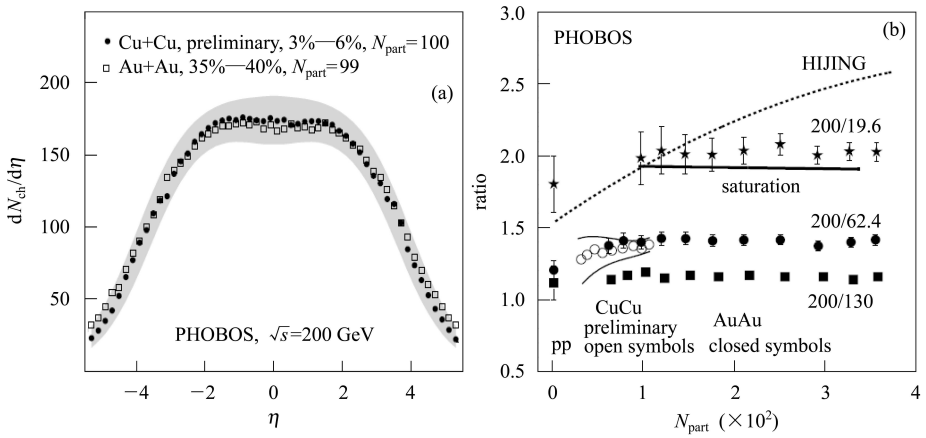

Fig. 34. (a) Pseudorapidity distribution for charged hadrons in Cu+Cu (closed symbols) and Au+Au collisions (open symbols) at $\sqrt{s_{\rm NN}}$ = 200 GeV. (b) Ratio of mid-rapidity densities as a function of $N_{\rm part}$.

$\sqrt{s_{\rm NN}}$ = 62.4 GeV has been measured with the PHOBOS detector at RHIC. The data are presented as a function of transverse momentum ($p_{\rm T}$) and collision centrality. The goal of these measurements is to study the modification of particle production in the presence of the produced medium by comparing with nucleon-nucleon collisions at the same energy[77].

In Fig. 35, PHOBOS presents the invariant yield of charged hadrons as a function of transverse momentum, obtained by averaging the yields of positive and negative hadrons. Data are shown for six centrality bins and are averaged over a pseudorapidity interval $0.2 < \eta < 1.4$.

Figure 36 shows the $p_{\rm T}$ distributions for pions, kaons, protons, and antiprotons in both central (top panel) and peripheral collisions (bottom panel) in PHENIX experiment[32]. The pion spectra have a concave shape at low $p_{\rm T}$ where many of the pions may come from the decay of resonances: Δ, ρ, etc. The kaon spectra are approximately exponential over the full measured $p_{\rm T}$ range, whereas the proton spectra flatten at low $p_{\rm T}$ for the most central collisions.

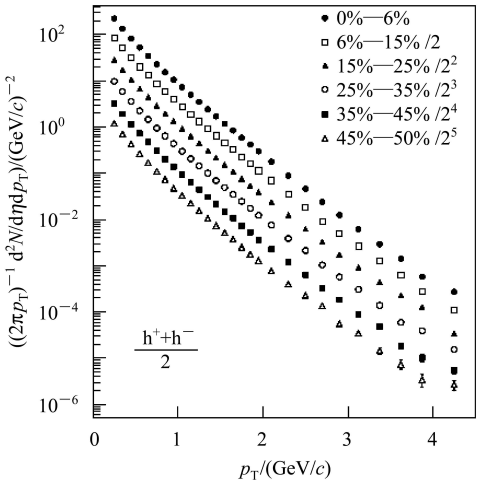

Fig. 35. Invariant yields for charged hadrons from Au+Au collisions at $\sqrt{s_{\rm NN}}$=62.4 GeV.

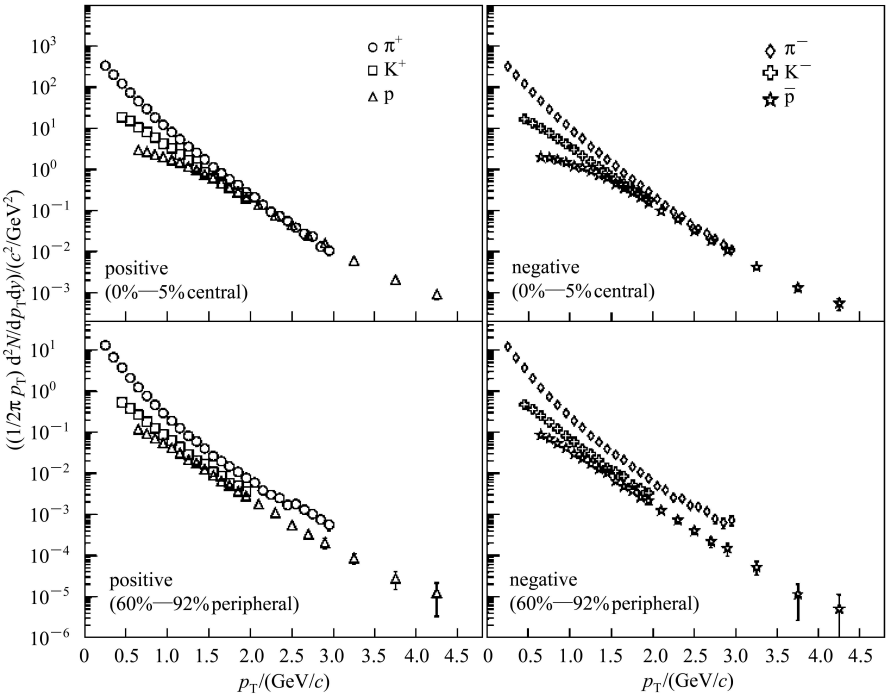

Fig. 36. Transverse momentum distributions for pions, kaons, protons, and antiprotons in Au+Au collisions at $\sqrt{s_{\rm NN}}$=200 GeV.

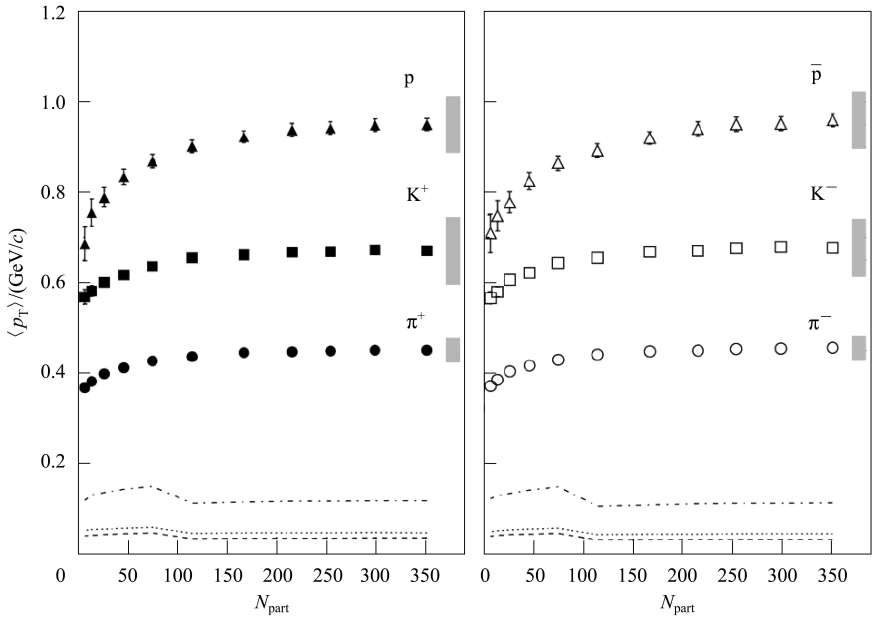

Fig. 37 $\langle p_{\rm T}\rangle$ of particles as a function of centrality ($N_{\rm part}$) in Au+Au collisions at $\sqrt{s_{\rm NN}}$ = 200 GeV.

The average transverse momentum, $\langle p_{\rm T}\rangle$, or the mean transverse kinetic energy, $\langle m_{\rm T}\rangle - m_0$, or the asymptotic slope are taken as measures of the temperature, T , of the reaction[78]. The $\langle p_{\rm T}\rangle$ of hadrons has a dependence of $N_{\rm part}$, as shown in Fig. 37[32].

The PHENIX results incontrovertibly demonstrate that there is a strong and centrality dependent suppression of the production of high-$p_{\rm T}$ pions relative to pQCD-motivated expectations. To better demonstrate the suppression, Fig. 38 shows $R_{\rm AA}(p_{\rm T})$ for mid-rapidity π^0's in central and peripheral 200 GeV Au+Au collisions[55], and also in d-Au collisions[79].

Figure 38 shows that the central Au+Au π^0 suppression changes only slightly over the measured $p_{\rm T}$ range and reaches an approximately $p_{\rm T}$-independent factor of 5 ($R_{\rm AA}\approx$0.2) for $p_{\rm T}$ >4—5 GeV/c. But we can not rule out a slight suppression by peripheral $R_{\rm AA}$. In all of the data sets $R_{\rm AA}$ increases with increasing $p_{\rm T}$ for $p_{\rm T} < 2$ GeV/c. Despite the differences

resulting from the protons, the charged particles and π^0's exhibit very similar trends in the suppression vs. $p_{\rm T}$ and vs. centrality. Meanwhile, no high $p_{\rm T}$ jet suppression is observed for d-Au collisions, and the $R_{\rm AA} > 1$ for $p_{\rm T}$ >4—5 GeV/c. To the further analysis for Fig. 38, we can get that the high-$p_{\rm T}$ yields of both charged hadrons and π^0's per participant increase proportional to $T_{\rm AB}$ for small $N_{\rm part}$ but level off and then decrease with increasing $N_{\rm part}$ in more central collisions.

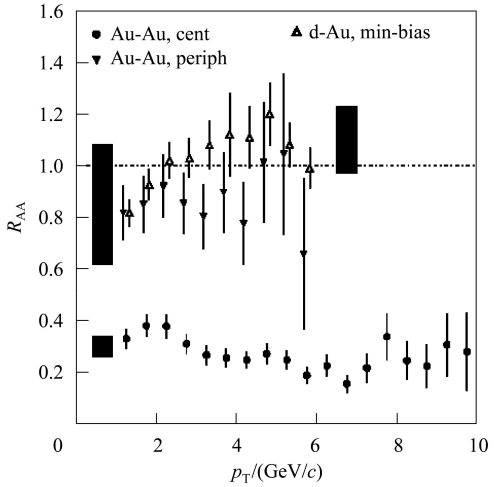

Fig. 38. π^0 $R_{\rm AA}(p_{\rm T})$ for central 0%—10% and peripheral 80%—92% Au+Au collisions and minimum-bias d-Au collisions.

Particle production at $p_{\rm T} > 1$ GeV/c in heavy-ion collisions is expected to be influenced by the interplay of many effects[77]. This includes $p_{\rm T}$ broadening due to initial and final state multiple scattering (the "Cronin effect"), the medium-induced energy loss of fast partons, and the effects of collective transverse velocity fields and of parton recombination[80].

The PHOBOS observations show that, surprisingly, the combination of all effects leads to a remarkably similar centrality evolution of the yields at high and low transverse momenta, providing a challenge to theoretical descriptions. That this is not accidental is suggested by the agreement with earlier measurements at $\sqrt{s_{\rm NN}}$ = 130 GeV. The lower energy data[81, 82], when compared over the same centrality range, show very similar centrality scaling, even though the yield at high $p_{\rm T}$ increases much more rapidly with increasing beam energy than the overall particle yield. It has recently been argued that the observed scaling could be naturally explained in a model assuming the dominance of surface emission of high $p_{\rm T}$ hadrons[83]. However, the approximate participant scaling has also been explained in the context of initial state saturation models[84], as shown in Fig. 39 where

$$R_{\rm AA}^{N_{\rm part}} = \frac{\sigma_{\rm pp}^{\rm inel}}{\langle N_{\rm part}/2\rangle} \frac{{\rm d}^2N_{\rm AA}/{\rm d}_{p_{\rm T}}{\rm d}\eta}{{\rm d}^2\sigma_{\rm pp}/{\rm d}_{p_{\rm T}}{\rm d}\eta}$$

and

$$R_{\rm PC}^{N_{\rm part}} = \frac{\langle N_{\rm part}^{0\%—6\%}\rangle}{\langle N_{\rm part}\rangle} \frac{{\rm d}^2N_{\rm AA}/{\rm d}_{p_{\rm T}}{\rm d}\eta}{{\rm d}^2N_{\rm AA}^{0\%—6\%}/{\rm d}_{p_{\rm T}}{\rm d}\eta}.$$

Data are shown in six bins of centrality, ranging from $\langle N_{\rm part}\rangle$=61 to 335 for 62.4 GeV collisions.

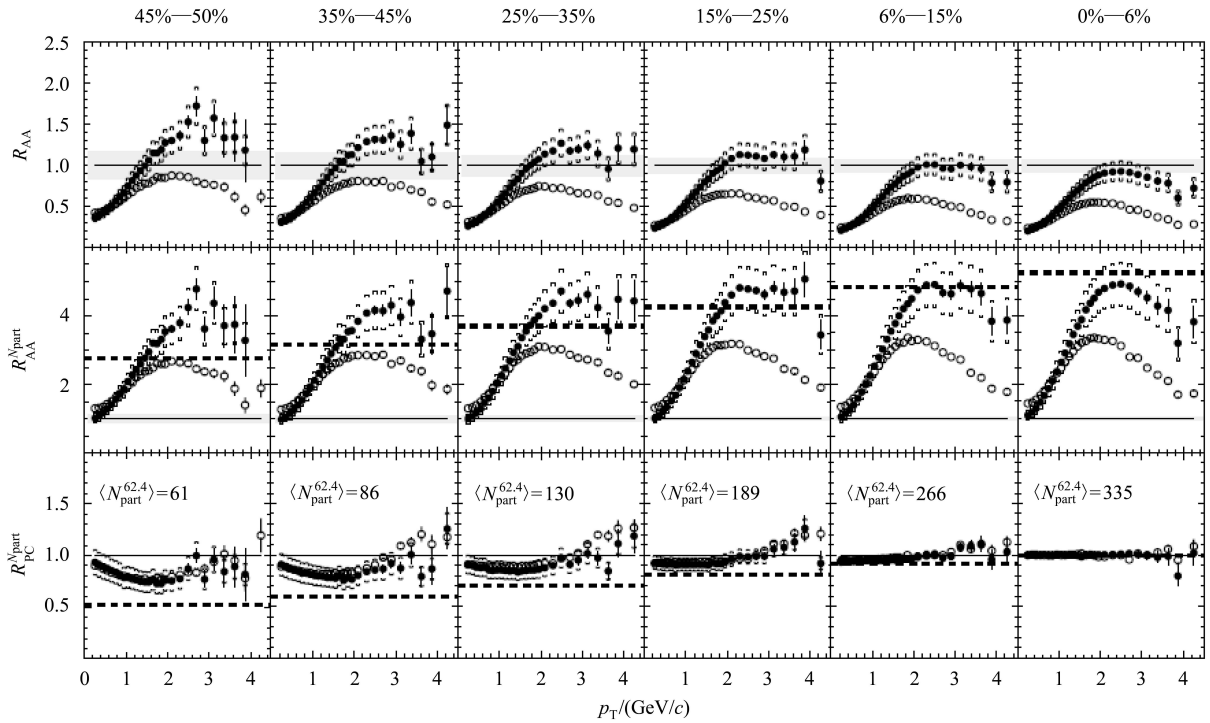

Fig. 39. Ratio of $p_{\rm T}$ distributions from Au+Au collisions to various reference distributions at $\sqrt{s_{\rm NN}}$=62.4 GeV (filled symbols) and 200 GeV (open symbols).

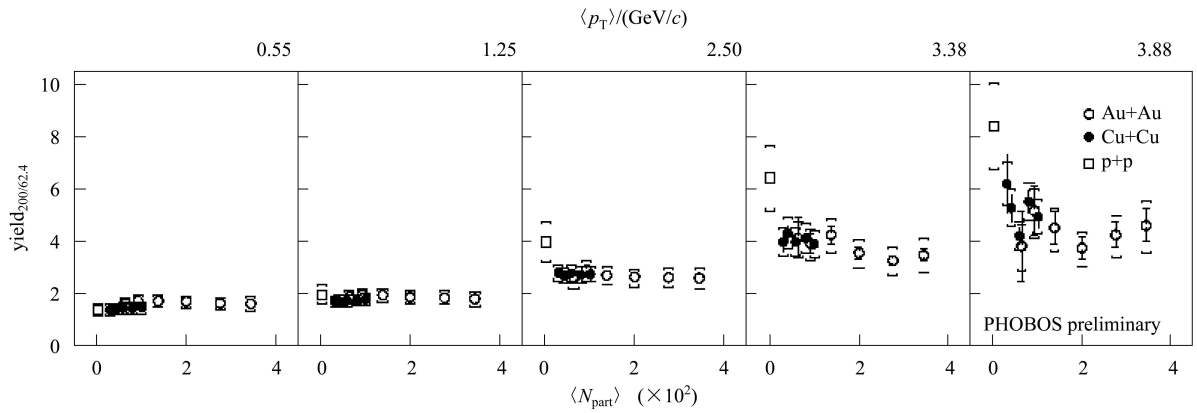

Fig. 40. Ratio of yields at $\sqrt{s_{NN}}$ = 200 GeV to 62.4 GeV for Cu+Cu (filled circles) and Au+Au (open circles).

As shown in Fig. 40, the ratio of yields in 200 GeV to 62.4 GeV is plotted versus centrality for a range of transverse momenta[85]. It shows that the ratio of yields in Cu+Cu has only a moderate centrality dependence and is consistent with the Au+Au value for all measured p_T .

The observed suppression of high-p_T particle production at RHIC is a unique phenomenon that has not been previously observed in any hadronic or heavy ion collisions at any energy. The suppression provides direct evidence that Au+Au collisions at RHIC have produced matter at extreme densities, greater than ten times the energy density of normal nuclear matter and the highest energy densities ever achieved in the laboratory[4].

4 Conclusion and outlook

Ultra-relativistic heavy ion collisions probably produce a new form of matter[86, 87]. So the general concepts to nuclear matter is not suitable any more, and need to discover new principles or mechanism[88]. In J. Zimányi's talk given at the 18th International Conference on Ultra Relativistic Nucleus-Nucleus Collisions[89], "Although theoretical models supported the early concept, the experimental data forced to change these speculations step by step."

After the overview of research status of soft physics in high energy heavy ion collision experiments, especially on basis of the recent experimental results, we try to give a conclusion as follows:

1) In central A+A collisions at RHIC energies, a high energy density medium is created. The energy density is estimated to be larger than 3 GeV/fm^3, which exceeds the critical energy density needed to form deconfined phase predicted by lattice QCD. As mentioned above, the RHIC experiments have discovered a new form of nuclear matter, "sQGP", which is strongly interactive, but not weakly interacting QGP.

2) The hydro approaches (Bjorken hydrodynamical model and Laudau hydrodynamical model) behave very well over a wide range of data. In p-p collisions, leading particle effect exists, flat distribution of x_F is nearly independent of energy, and only about 50% of energy is available for particle production. But the leading particle effect is suppressed in A+A collisions in high p_T range (not appeared in p-p collisions), and about 70%—80% of energy is available for particle production. Stopping effect in A+A collisions is comparable with expectations from p-A collisions.

3) Many of the experimental data can be expressed in terms of simple scaling behaviors. In particular, the data clearly demonstrate that proportionality to the number of participating nucleons, N_{part}. The total multiplicity and charged particle density per participant from different systems are close to identical when compared at the same available energy, and many characteristics of the produced particles factorize to a surprising degree into separate dependence on centrality and beam energy. This feature of multiplicity in A+A, p-p and e^+e^- collisions is possibly caused by parton saturation effect. The limiting fragmentation scaled by N_{part} is not independent of centrality at high pseudorapidity, and grows in pseudorapidity extent with beam energy. The experimental data from LHC, will help to further evaluate the range of validity of these scaling behaviors.

In Dr. T.D. Lee's overview[90], "The strongly interactive quark-gluon plasma can be produced by Au+Au collisions at RHIC. Therefore it will be produced at LHC. Since sQGP is produced by deutron-Au collisions at RHIC (in the forward direction), it will also be produced through p-p collisions at LHC. This begins a new era of physics."

Starting in 2007 the LHC will collide the proton beams at $\sqrt{s}$=14 TeV and the lead beams at $\sqrt{s_{NN}}$=5.5 TeV, and the luminosity of these two colli-

sion mode is 5×10^{30} and 5×10^{26} $\mathrm{cm^{-2}\cdot s^{-1}}$ respectively. The center of mass energy for collisions of the heaviest ions at the ALICE will exceed that available at BNL/RHIC by a factor of about 30[91]. Collisions at these previously un-explored energies offer opportunities to create extreme conditions which are higher energy densities (in the regime $\varepsilon \approx 1$—$1000\ \mathrm{GeV/fm^3}$), larger volumes and longer timescales than in RHIC. ALICE is a general-purpose heavy ion experiment designed to study the physics of strongly interacting matter and the QGP in nucleus-nucleus collisions at the LHC[6]. The unique capabilities include its low transverse momentum (p_T) acceptance, excellent vertexing, particle identification over a broad p_T range and jet reconstruction[6, 92, 93].

1) The $\mathrm{d}N_\mathrm{ch}/\mathrm{d}y$ could reach up to 2×10^3—8×10^3, which is the most fundamental observable to investigate properties of the medium created in the collisions. The charged particle rapidity density is expected to follow Feynman scaling with $\sqrt{s}$, and the multiplicity distribution is expected to show strong departure from KNO scaling. All of these can be studied by ALICE.

2) ALICE experiment measures and identifies particles over a wide p_T range (from 100 MeV/c to 100 GeV/c). Studies on p_T spectra are important to understand any new physics at LHC energies.

3) ALICE can measure and identify photons over a large p_T range with Photon Spectrometer (PHOS). Measurements of inclusive and direct photons are important signatures of QGP probing and initial information of the collisions.

LHC is scheduled to deliver p-p beams at $\sqrt{s}$=900 GeV late this year, possibly 14 TeV in 2008, and Pb+Pb beams at 5.5 TeV in 2008. The LHC/ALICE will certainly open up new aspects of physics for us.

As analysis work for the RHIC's first three run and SPS data, physical scientists have been achieving many great results, and finding many signatures of QGP, phase transition and deconfinement of color. However, the research for these physical goals is just on the way. The RHIC and GSI are currently updating their detectors, and many accelerators are planning to be established in many countries. Absolutely, to us the most expecting experiment in the near future is LHC at CERN. We are looking forward to the exciting experimental data of the first p-p collisions at 900 GeV from LHC/ALICE. It will help us to have a further and deeply understanding of the properties of the QGP state, QCD phase transition and chiral-symmetry restoration.

References

1 Arsene I et al. (BRAHMS collaboration). Nucl. Phys. A, 2005, **757**: 1—27
2 Back B B et al. (PHOBOS Collaboration). Nucl. Phys. A, 2005, **757**: 28—101
3 Adams J et al. (STAR Collaboration). Nucl. Phys. A, 2005, **757**: 102—183
4 Adcox K et al. (PHENIX Collaboration). Nucl. Phys. A, 2005, **757**: 184—283
5 Huovinen P, Ruuskanen P V. Annual Review of Nuclear and Particle Science, 2006, **56**: 163—206
6 Carminati F et al. (ALICE Collaboration). J. Phys. : Nucl. Part. Phys. G, 2004, **30**: 1517—1763
7 Karsch F et al. Nucl. Phys. B (Proc. Suppl.), 2000, **83-84**: 390—392; Phys. Lett. B, 2000, **478**: 447—455. arXiv: hep-lat/0305025
8 Ulrich Heinz. arXiv: hep-ph/0407360
9 Alper B et al. Nucl. Phys. B, 1975, **100**: 237—290
10 Albajar C et al. Nucl. Phys. B, 1990, **335**: 261
11 Abe C et al. Phys. Rev. Lett., 1988, **61**: 1818
12 ZHOU Dai-Mei, WANG Ya-Ping, WEI Li-Hua et al. "Correlations and Fluctuations in High Energy Heavy Ion Collision Experiments", in press by Chin. Phys. C (HEP & NP); WANG Ya-Ping, ZHOU Dai-Mei, CAI Xu. "Collective Expansion and Hadronization in High Energy Heavy Ion Collision Experiment", in press by Chin. Phys. C (HEP & NP)
13 CAI Xu, ZHOU Dai-Mei. HEP & NP, 2002, **26**(9): 971—990 (in Chinese)
14 Steinberg P A. Nucl. Phys. A, 2005, **752**: 423c—432c
15 Landau L D. Izv. Akad. Nauk Ser. Fiz., 1953, **17**: 51
16 Belenkij S Z et al. Nuovo Cim. Suppl., 1956, **3S10**: 15
17 Back B B et al. (PHOBOS Collaboration). arXiv: nucl-ex/0301017
18 Steinberg P. Acta Phys. Hung. A, 2005, **24**: 51—57
19 Bearden I G et al. (BRAHMS Collaboration). Phys. Rev. Lett., 2005, **94**: 162301
20 Kolb P F, Heinz U. arXiv: nucl-th/0305084
21 Bjorken J D. Phys. Rev. D, 1983, **27**: 140
22 Feynman R P. Phys. Rev. Lett., 1969, **23**: 1415
23 Hirano T. Phys. Rev. C, 2002, **65**: 011901
24 Roland G et al. (PHOBOS Collaboration). Nucl. Phys. A, 2006, **774**: 113—128
25 Bearden I G et al. (BRAHMS Collaboration). Phys. Rev. Lett., 2002, **88**: 202301
26 Busza W. Acta Phys. Pol. B, 1977, **8**: 333
27 Back B B et al. (PHOBOS Collaboration). Phys. Rev. Lett., 2002, **88**: 022302
28 Adcox K et al. (PHENIX Collaboration). Phys. Rev. Lett., 2001, **87**: 052301
29 Adams J et al. (STAR Collaboration). Phys. Rev. C, 2004, **70**: 054907
30 Back B B et al. (PHOBOS Collaboration). Phys. Lett. B, 2004, **578**: 297
31 Back B B et al. (PHOBOS Collaboration). Phys. Rev. C, 2004, **70**: 051901(R)
32 Adler S S et al. (PHENIX Collaboration). Phys. Rev. C, 2004, **69**: 034909
33 Fischer H G et al. (NA49 Collaboration). Nucl. Phys. A, 2003, **715**: 118
34 Dezsö Varga. (NA49 Collaboration). Hadron-Nucleus Collisions as a Laboratory for the Study of Multiple Soft Hadronic Interactions, submitted to World Scientifc, 2004
35 Appelshäuser H. (NA49 Collaboration). Phys. Rev. Lett., 1999, **82**: 2471—2475
36 Bearden I G et al. (BRAHMS Collaboration). Phys. Rev. Lett., 2004, **93**: 102301

37 Bass S A et al. Nucl. Phys. A, 1999, **661**: 205
38 Soff S et al. Phys. Lett. B, 2003, **551**: 115
39 Bass S A et al. Phys. Rev. Lett., 2003, **91**: 052302
40 Benecke J et al. Phys. Rev., 1969, **188**: 2159
41 GŚbor I. Veres. Nucl. Phys. A, 2006, **774**: 287—296
42 Peter Steinberg. arXiv: nucl-ex/0702020
43 Abe F et al. (CDF Collaboration). Phys. Rev. D, 1990, **41**: 2330
44 Ansorge R E et al. (UA5 Collaboration). Z. Phys. C, 1989, **43**: 75
45 Thome W et al. (ISR Collaboration). Nucl. Phys. B, 1977, **129**: 365
46 Abreu P et al. (DELPHI Collaboration). Phys. Lett. B, 1999, **459**: 397
47 Back B B et al. (PHOBOS Collaboration). Phys. Rev. C, 2005, **72**: 031901
48 Arsene I et al. (BRAHMS Collaboration). Phys. Rev. Lett., 2005, **94**: 032301
49 Back B B et al. (PHOBOS Collaboration). Phys. Rev. Lett., 2003, **91**: 052303
50 Basile M et al. Il Nuovo Cimento A, 1981, **66**: 129
51 Steinberg Peter A et al. (PHOBOS Collaboration). Nucl. Phys. A, 2003, **715**: 490c—493c
52 Basile M et al. Phys. Lett. B, 1980, **92**: 367
53 Basile M et al. Phys. Lett. B, 1980, **95**: 311
54 Adams J et al. (STAR Collaboration). Phys. Rev. Lett., 2003, **91**: 172302
55 Adler S S et al. (PHENIX Collaboration). Phys. Rev. Lett. C, 2003, **91**: 072301; Phys. Rev. C, 2004, **69**: 034910
56 Dainese A et al. Acta Phys. Hung. A, 2006, **27**: 245—249
57 WANG X N et al. Phys. Rev. D, 1992, **45**: 844
58 Alner G J et al. Z. Phys. C, 1986, **33**: 1
59 Deines-Jones P et al. Phys. Rev. C, 2000, **62**: 014903
60 Bearden I G et al. Phys. Lett. B, 2001, **523**: 227
61 Back B B. J. Phys. Conf. Ser., 2005, **5**: 1—16
62 Back B B et al. (PHOBOS Collaboration). Phys. Rev. Lett., 2000, **85**: 3100—3104
63 Bialas A et al. Nucl. Phys. B, 1976, **111**: 461
64 Eskola K J. Nucl. Phys. A, 2002, **698**: 78c
65 Adler S S et al. (PHENIX Collaboration). Phys. Rev. C, 2005, **71**: 034908
66 Back B B et al. (PHOBOS Collaboration). Phys. Rev. C, 2002, **65**: 061901
67 Baker M D et al. (PHOBOS Collaboration). Nucl. Phys. A, 2003, **715**, 65c
68 Ullrich T S. (STAR Collaboration). Heavy Ion Phys., 2004, **21**: 143
69 Ullrich T S. (STAR Collaboration). Nucl. Phys. A, 2003, **715**: 399
70 Adams J et al. (STAR Collaboration). Phys. Rev. Lett., 2005, **95**: 062301
71 Back B B et al. (PHOBOS Collaboration). arXiv:nucl-ex/0604017
72 Alner G J et al. Phys. Rep., 1987, **154**: 247
73 Heiselberg H. Phys. Rep., 2001, **351**: 161
74 Alner G J et al. Phys. Lett. B, 1986, **167**: 476
75 Back B B et al. (PHOBOS Collaboration). Phys. Rev. C, 2004, **70**: 021902
76 Constantin Loizides. (PHOBOS Collaboration). arXiv:nucl-ex/0605012
77 Back B B et al. (PHOBOS Collaboration). Phys. Rev. Lett., 2005, **94**: 082304
78 Tannenbaum M J. arXiv: nucl-ex/0702028
79 Adler S S et al. (PHENIX Collaboration). Phys. Rev. Lett., 2003, **91**: 072303
80 Jacobs P et al. Prog. Part. Nucl. Phys., 2005, **54**: 443
81 Adler C et al. Phys. Rev. Lett., 2002, **89**: 202301
82 Adcox K et al. Phys. Lett. B, 2003, **561**: 82
83 Müller B. Phys. Rev. C, 2003, **67**: 061901
84 Kharzeev D et al. Phys. Lett. B, 2003, **561**: 93
85 Edward Wenger. (PHOBOS Collaboration). Acta Phys. Hung. A, 2006, **27**: 271—274
86 CAI Xu. Progress in Physics, 1988, **8**: 186 (in Chinese)
87 CAI Xu. Science Foundation in China, 1992, **6**(1): 46; 1994, **8**(2): 98; 1994, **2**(2): 44 (in Chinese)
88 WANG Ya-Ping, CAI Xu. HEP & NP, 2006, **30**(12): 1218—1221 (in Chinese)
89 Zimányi J. Nucl. Phys. A, 2006, **774**: 25—34
90 Lee T D. Nucl. Phys. A, 2005, **750**: 1—8
91 WANG Ya-Ping, CAI Xu. HEP & NP, 2006, **30**(7): 606—6111 (in Chinese)
92 Tapan K. Nayak. (ALICE Collaboration). J. Phys. G: Nucl. Part. Phys., 2007, **34**: S783—S787
93 Alessandro B et al. (ALICE Collaboration). J. Phys. G, 2006, **32**: 1295—2040